Journal Pre-proof

Combining traditional and quantitative multiscale structural analysis to reconstruct the tectono-metamorphic evolution of migmatitic basements: The case of the Valpelline Series, Dent-Blanche Tectonic System, Western Alps

F. Caso, C.B. Piloni, M. Filippi, A. Pezzotta, E. Fazio, R. Visalli, G. Ortolano, M. Roda, M. Zucali

PII: S0191-8141(24)00051-8

DOI: https://doi.org/10.1016/j.jsg.2024.105099

Reference: SG 105099

To appear in: *Journal of Structural Geology*

Received Date: 28 August 2023

Revised Date: 18 January 2024

Accepted Date: 7 March 2024

Please cite this article as: Caso, F., Piloni, C.B., Filippi, M., Pezzotta, A., Fazio, E., Visalli, R., Ortolano, G., Roda, M., Zucali, M., Combining traditional and quantitative multiscale structural analysis to reconstruct the tectono-metamorphic evolution of migmatitic basements: The case of the Valpelline Series, Dent-Blanche Tectonic System, Western Alps, *Journal of Structural Geology* (2024), doi: https://doi.org/10.1016/j.jsg.2024.105099.

Combining traditional and quantitative multiscale structural analysis to reconstruct the tectono-metamorphic evolution of migmatitic basements: the case of the Valpelline Series, Dent-Blanche Tectonic System, Western Alps

Caso F.[a*], Piloni C.B.[a], Filippi M.[a], Pezzotta A.[a], Fazio E.[b], Visalli R.[b], Ortolano G.[b], Roda M.[a], Zucali M.[a]

[a]Department of Earth Sciences "A. Desio", University of Milan, Via Mangiagalli 34, 20133 Milan, Italy

[b]Department of Biological, Geological and Environmental Sciences, University of Catania, Catania, Italy

*corresponding author: fabiola.caso@unimi.it

Keywords: 3D outcrop models; quantitative multiscale structural analysis; X-ray maps; high-temperature deformation; migmatites

Abstract

Due to the ongoing development of new technologies, many instruments are available to assist geological investigations at different scales. These techniques, including 3D outcrop modelling from aerial photogrammetry, and quantitative microstructural analysis are useful in crystalline basement studies. This contribution combines traditional and quantitative multiscale structural analysis techniques to the migmatitic rocks of the Valpelline Series (Dent-Blanche Tectonic System, Western Alps). Conventional structural analysis is integrated with the extraction of structural data from 3D models of representative smooth outcrops. Quantitative microstructural and mineral-chemical analyses are combined to link structural and metamorphic evolution. This approach allows identifying and correlating foliations that developed during three tectono-metamorphic stages. The first (D_1) includes solid-state deformation associated with an early foliation (S_1) preserved within metabasite boudins enclosed in migmatite gneiss. The second (D_2) is related to the dominant foliation in migmatite gneiss (S_2), coeval with the regional scale anatexis and growth of garnet and cordierite. The third (D_3) is related to the late folding of S_2 and the development of a sillimanite-rich axial plane foliation (S_3) which wraps around garnet and cordierite. Finally, this work discusses pros and cons of

each innovative methodology, still emphasising the importance of using manual field data as ground control.

1. Introduction

In the last two decades, new methods including remote sensing techniques and on-field data acquisition using smartphones and tablets (e.g., Lee et al., 2013; Field-Move app; Midland Valley, 2015), are changing the way geoscientists collect data in the field (e.g., Zerboni et al., 2015; Tavani et al., 2022; Misra and Mukherjee, 2023). In particular, there is a growing accessibility to high-resolution satellite imagery (e.g., Perego et al., 2011), and it is relatively easy to acquire photogrammetric images using different instruments. These range from digital cameras equipped with LiDAR (Laser Imaging Detection and Ranging) sensors to UAVs (Unmanned Aerial Vehicles). The development of relatively small and low-cost UAVs permits the high-resolution mapping of areas and their 3D reconstruction, especially when no LiDAR data can be retrieved (e.g., Forti et al., 2023). One of the most common techniques of digital photogrammetry is the Structure from Motion (SfM), which permits to reconstruct a 3D structure from bidimensional photographs. The 3D models obtained by these techniques encompass valuable data for structural geology (e.g., Tavani et al., 2014; 2016; Cawood et al., 2017; Mattéo et al., 2021), geomorphology (Bonasera et al., 2022, 2023; Misra and Mukherjee, 2023), and archaeometry (Brandolini et al., 2020). All these approaches are particularly effective in Alpine environments undergoing deglaciation, where the absence of vegetation cover and the smoothness of the outcrops permit a clear exposure of rocks and structures.

Many studies used these techniques to extract structural data such as orientations of foliation surfaces, fold axes, and fractures. The results remain reliable even when compared to handheld measured data, typically exhibiting a mismatch of approximately 5° in dip values and 10°–15° in dip azimuth (e.g., Cawood et al., 2017; Novakova and Pavlis, 2017). This approach may be particularly useful in such environments where obtaining a statistically significant number of orientations for structural calculations (e.g., fold analysis, fractures analysis; Ramsey and Huber, 1987; Cawood et al., 2017)

may be complex due to several factors. These include (i) the geographical location of the outcrops at high altitudes and/or with snow coverage, making them accessible only for a few months during the year and only a few hours a day; (ii) outcrops located on vertical cliffs that are completely inaccessible for traditional data measurements and sampling. In these situations, aerial photogrammetry with drones and/or 3D outcrop modelling through cameras equipped with LiDAR sensors are very helpful. Indeed, this approach allows also to extend the dimensions of the study area up to the hectometer scale.

In the last years, several innovative methodologies have been also improved for microstructural and mineral-chemical analysis of crystalline basements (e.g., Corti et al., 2019; Visalli et al., 2021; Zucali et al., 2021; Caso, 2023; Fazio et al., 2024) that are facilitating the quantitative digital transition of fabric and petrological rock parameters acquisition. These techniques include the extraction of quantitative grain shape parameters from thin sections by semi-automatic segmentation (Heilbronner, 2011; Heilbronner and Barrett, 2014; Corti et al., 2019; Visalli et al., 2021) and quantitative chemical data extraction from Electron MicroProbe Analyser (EMPA) X-ray maps and point mineral-chemical analyses (e.g., XMapTools; Lanari et al., 2014; Q-XRMA; Ortolano et al., 2018). The combination of these two techniques is effective in discriminating different generations of superimposed structures and defining tectono-metamorphic stages (e.g., Corti et al., 2019; Roda et al., 2021; Zucali et al., 2021; Caso, 2023).

The goal of this work is to combine these analysis techniques developed to operate at different scales. Indeed, a reliable reconstruction of the tectono-metamorphic evolution of crystalline basements requires a multiscale approach to collect and analyse structural data, specifically foliations and folds associated with superimposed deformation stages. In this situation, is also fundamental the identification of the mineral assemblages supporting each structure (e.g., Spalla, 1993; Johnson and Vernon, 1995; Zucali et al., 2002; Passchier and Trouw, 2005; Spalla et al., 2005). Moreover, these techniques aid in the targeted choice of meso- and microstructural domains with different deformation

and metamorphic transformation degrees (e.g., coronitic, tectonitic and mylonitic domains; Salvi et al., 2010; Gosso et al., 2015; Zucali et al., 2020), aimed at reconstructing the whole tectono-metamorphic history.

The use of modern quantitative techniques may be particularly useful in the study of migmatitic basement rocks, characterised by complex structural patterns derived from the interplay between metamorphic, magmatic, and deformative processes under transient conditions (Brown, 1973; Hopgood, 1979; Ashworth, 1985; Kreigsman, 2001; Sawyer, 2001, 2008; Kreigsman and Alvarez-Valero, 2010; Yakimchuk, 2020). In fact, multiple partial melting events and the complex geometrical patterns resulting from melt migration (Sawyer, 2001) complicate the reconstruction of the tectono-metamorphic evolution of these basements. Consequently, it is often difficult to reconstruct the relative chronology of the deformation events during high-temperature (H*T*) evolution through traditional "field-based only" structural analysis. However, a multidisciplinary and multiscale approach that combines meso- and microscale analysis supported by mineral-chemical data using different new approaches is still missing.

Therefore, in this study, we choose the migmatitic basement of the Valpelline Series (Dent-Blanche Nappe, Western Italian Alps) as a case study, to envisage a comprehensive view of its structural and tectono-thermal evolution. This series represents a fragment of the pre-Alpine lower continental crust that underwent H*T* deformation and partial melting during Permian lithospheric extension (Zucali et al., 2011; Pesenti et al., 2012; Manzotti and Zucali, 2013, Caso, 2023; Caso et al., 2024).

2. Geological setting

The Alps (Fig. 1a) are one of the peri-Mediterranean mountain ranges originated from the subduction of the Ligurian-Piedmont Ocean during the Cretaceous and collision between the Adria and European plates in the Eocene (Dewey et al., 1989; Schmid et al., 2004; Beltrando et al., 2010; Handy et al., 2010; Lardeaux, 2014; Angrand and Mouthereau, 2021). The Austroalpine and Penninc domains

constitute the axial zone of the Alps, whose oceanic and continental rocks underwent high-pressure and low-temperature metamorphism during the Alpine subduction.

The Dent-Blanche Tectonic System (DBTS; Manzotti et al., 2014a; Manzotti and Ballèvre, 2017) belongs to the Austroalpine domain and overlies the oceanic units. The DBTS is traditionally divided into the Dent-Blanche s.s. to the northwest and the Mont-Mary Nappe to the southwest separated by a km-scale mylonitic zone, the Roisan-Cignana Shear Zone (RCSZ, Fig. 1b; Zucali et al., 2011; Manzotti et al., 2014a, b). The Dent-Blanche s.s consists of a Paleozoic basement corresponding to the Arolla and the Valpelline series (Diehl et al., 1952; Manzotti and Zucali, 2013; Manzotti et al., 2014a) which recorded both pre-alpine and alpine metamorphism. The Arolla Series is made of Permian metagranitoid, metagabbro and pre-Permian lenses of migmatite gneiss. Alpine metamorphism and deformation are more pervasive in the Arolla Series than in the Valpelline Series. In particular, in the Arolla Series the Alpine metamorphism developed under blueschists-facies conditions (Roda and Zucali 2008; 2011; Manzotti et al., 2014a, b; Manzotti et al., 2020). Conversely, the Valpelline Series (VP) better preserves Permian structures and metamorphic assemblages (Zucali et al., 2011; Pesenti et al., 2011; Kunz et al., 2018) from the amphibolite- to granulite-facies conditions (Gardien et al., 1994; Manzotti and Zucali, 2013; Caso, 2023; Caso et al., 2024).

Insert Figure 1 here.

The VP consists of migmatitic metapelites, as Grt–Crd- (abbreviations hereafter are according to Whitney & Evans, 2010) and Grt–Opx-migmatite gneiss, and sillimanite-gneiss, plus felsic granulite. Metasedimentary and felsic rocks are associated with Grt–Cpx-amphibolite also locally affected by partial melting (black amphibolite in Fig. 2a), minor pegmatites and aplites, basic granulites and marbles (Diehl et al., 1952; Nicot, 1977; Gardien et al., 1994; Manzotti and Zucali, 2013; Caso et al., 2024). In the VP a former tectono-metamorphic stage (pre-D_2 in Manzotti and Zucali, 2013) is marked by a relict foliation preserved in meter-scale metabasite bodies. This stage has developed at T = 700±50°C and P = 0.57±0.11 GPa (Manzotti and Zucali, 2013). Conversely, Gardien et al. (1994)

125 estimated higher pressure conditions within the kyanite stability field (T = 700–800°C and P = 0.9–
126 1.0 GPa) for the pre-D_2 stage preserved within garnet cores. D_2 stage is related to the development of
127 the regional foliation S_2 and widespread melting, at T = 810±40°C and P = 0.7±0.01 GPa (Gardien et
128 al. 1994; Manzotti and Zucali, 2013). S_2 is parallel to the lithological boundaries and strikes NE–SW
129 dipping at high angles. During a later stage (T = 800±30°C and P = 0.6±0.07 GPa; D_3 in Manzotti
130 and Zucali, 2013), the S_2 is folded, leading to the local development of an S_3 axial plane foliation,
131 marked by the blastesis of biotite and sillimanite both at the meso- and microscale. Gardien et al.
132 (1994) recognised a further migmatitic stage related to the cordierite growth, estimated at T = 650–
133 700°C and P = ~0.35–0.45 GPa. However, recent microstructural analyses found the presence of
134 cordierite within melt-rich portions developed during D_2 and wrapped by S_3 sillimanite-rich foliation
135 (Caso et al., 2024).

136 The Alpine deformation in the VP is localized in decameter- to hectometer-wide shear zones (crossed
137 patterns in Figure 2a) marked by cataclasites and mylonites (Pennachioni and Guermani, 1993; Roda
138 and Zucali, 2008; Manzotti and Zucali, 2013). The mylonitic foliation is marked by chlorite and white
139 mica and developed under greenschists-facies conditions (T = 430±30°C and P = 0.3–0.5 GPa;
140 Gardien et al., 1994; Manzotti and Zucali, 2013). Mylonitic rocks occurring at contact with the Arolla
141 Series may be contemporaneous to the RCSZ shearing, under blueschists-facies conditions (D_3-D_4
142 stages in Manzotti et al., 2014b). Late stages of Alpine deformation (see D_5 stage in Manzotti et al.,
143 2014b) may be also responsible for the change in orientations of pre-Alpine S_2 and S_3 foliations in
144 the VP, approaching Arolla Series and RCSZ (Dal Piaz et al., 2016; Manzotti et al., 2014b). The
145 precise age of the Alpine metamorphism in the VP is not well-constrained. The whole-rock Rb/Sr
146 ages of Alpine mylonites at the contact between the Arolla and Valpelline series are of ~57 Ma
147 (Angiboust et al., 2014).

148 *Insert Figure 2 here.*

149 **3. Methods**

3.1 Mesoscale structural analysis

Mesoscale structural analysis has been conducted by combining traditional field observations and measurements with the extraction of data, from UAVs flights and LiDAR point clouds, of the main fabric elements (foliations and dykes orientations). In particular, the orientations of foliations, aplites and pegmatites have been firstly acquired with the compass on the field, together with rock sampling of representative migmatite gneiss for a better constrain of the remote data acquisition. This approach was used in clear and smoother outcrops which represent ideal case studies for 3D outcrop modelling.

SfM technique permitted to develop a 3D model of the selected areas in the VP from 2D images georeferenced in WGS84 coordinates system retrieved with UAV (Westoby et al., 2012; Niedzielski, 2018). The area covered by UAV flight is approximately 40,000 m^2, located at the Lac Mort (see the yellow square in Fig. 2a; coordinates: x: 382627; y: 5086138; z: 2850 m a.s.l.), on the right slope of the Place Moulin creek Valley. Flights at 15 and 30 m height were made using a Parrot® Anafi drone equipped with a 4k/21 MP camera (Fig. 3a), for the acquisition of ~380 photos, with a resolution of 5344*4016 pixels. After that, the photos have been uploaded in Agisoft Metashape version 1.5.5 software (Agisoft Metashape, 2023), and automatically aligned and processed to obtain a point cloud and a mesh model.

Selected outcrops of this area have been scanned through an iPad 11'' Pro equipped with a LiDAR sensor, using the 3D scanner App©, which directly produces a 3D model from a point cloud (Fig. 3b). Both the point clouds derived from the SfM and LiDAR scanning have been exported, reprojected in coordinate metric system (WGS84 – UTM32N) and processed within the CloudCompare software version 2.13 (CloudCompare, 2023), to extract the orientation of the main structural elements. The CloudCompare *Compass* plug-in (Thiele et al., 2017) permits tracing the upper and lower boundaries of a structural element (e.g., including dykes and layers) and produces an interpolated plane that has its dip direction and dip angle (Fig. 3c). Then, the so-obtained structural data were extracted from the software and projected on equal areal stereo plots, together with compass

175 measures, to increase the total number of available structural data and using manual measures as
176 ground control.

177 The traces of dykes visible from the Google Satellite© imagery were traced and grouped in a vector
178 polyline layer (Fig. 3d), and processed through the *Qgsurf* plug-in
179 (https://gitlab.com/mauroalberti/qgSurf) in QGIS version 3.22 (QGIS Development Team, 2023).
180 This tool, using the DEM (Digital Elevation Model) as a base, allowed us to obtain the dip direction
181 and dip angle of a plane which represent the best fit of each traced line intersecting the topographic
182 surface. Then, the data were plotted in an equal areal stereo plot as strikes of the lines calculated from
183 the dip directions.

184 *Insert Figure 3 here.*

185 *3.2 Microscale structural analysis*

186 Two samples for quantitative microstructural analysis have been chosen after analysing at the optical
187 microscope dozens of different migmatite gneiss from different localities of the VP. The chosen
188 samples show different modal proportions, mineral phase distributions and structures. In particular,
189 one sample is representative of a melanosome, and one is representative of a leucosome (33SC and
190 VP34 respectively; see samples location in Fig. 2a), both corresponding to cordierite-migmatite
191 gneiss. First, they were analysed with the optical microscope for the reconstruction of the
192 microstructural relations between the different mineral phases, and to define the mineral assemblages
193 marking each recognised fabric element (Passchier and Trouw, 2005; Spalla et al., 2005). The
194 quantitative microstructural analysis was carried out through the Micro-Fabric Analyzer ArcGis
195 toolbox (MFA; Visalli et al., 2021; Fig. 4), used to obtain the vectorial contouring of the mineral
196 grains and measure their shape parameters (see Visalli et al., 2021 Appendix A for the explanation of
197 the calculated values).

198 In detail, the MFA toolbox comprises and uses: (i) the Grain Size Detector (GSD; Fig. 4) which traces
199 vectorial polygonal grains contouring maps by processing and segmenting a high-resolution optical
200 thin section scan (Fig. 4; Visalli et al., 2021); (ii) the Quantitative X-Ray Maps Analyzer tool (Q-
201 XRMA; Ortolano et al., 2018) which derived a mineral classification map obtained from X-ray maps
202 processing (first cycle); (iii) the Mineral Grain Size Detector (Min-GSD; Visalli et al., 2021) which
203 allows merging the outputs of the GSD and Q-XRMA to label each grain polygon feature with its
204 mineral phase name, since the GSD tool does not separate the grains into different minerals. To apply
205 the latter tool is necessary to geo-reference in ArcGIS the Q-XRMA output on the GSD one. Both
206 the MFA and Q-XRMA toolboxes have been developed at the Geoinformatics and Image Analysis
207 Lab of the Biological, Geological, and Environmental Sciences Department at the University of
208 Catania (Italy).

209 The thin section scans used in the GSD toolbox were acquired under crossed polarized light by using
210 an Epson V750 dual-lens system scanner at 24 bit-depth and 4800 dpi of resolution corresponding to
211 a pixel size of ~5.29 µm. These settings for this device represent the best compromise between high-
212 quality imaging, relatively fast image-processing time, and reasonable hard drive space storage
213 (Visalli et al., 2021).

214 Among the obtained shape parameters, the long axis orientation (values between 0° – 180°) and the
215 roundness (see Supplementary Material 1 for all the obtained shape parameters) have been used for
216 the distinction of different microstructures marked by different mineral generations. In particular, the
217 long axis orientation is the angle between a vertical reference (in this case roughly perpendicular to
218 the main foliation of the thin section, depending on the thin section scan orientation) and the long
219 axis of each mineral grain, measured clockwise. Therefore, in this case, grains marking the main
220 foliation will have orientations of ~90°.

221 *3.2.1 Mineral-chemical analysis*

Quantitative mineral-chemical points analysis and X-ray chemical maps of major (Si, Ti, Al, Fe, Mn, Mg, Ca, Na, K) and minor elements (Cr) have been acquired using the Electron Microprobe Analyser (EMPA) JEOL 8200 Superprobe WDS at the Dipartimento di Scienze della Terra "A. Desio" – Università degli Studi di Milano. For sample 33SC the Fe, Mg, Ti, Ca and Na maps were acquired using five wavelength-dispersive spectometers (WDS) detectors, while Si, Al, Mn, Cr and K maps using an energy-dispersive spectrometer (EDS) detector. These maps were acquired using a beam current of 100 nA, with a dwell time of 55 ms and a resolution 1024*600 pixels (35 µm of step size). For sample VP34 four element maps were acquired (Al, Fe, K, Na) using four WDS detectors. These maps were acquired using a beam current of 50 nA, a dwell time of 15 ms and a resolution of 1024*512 pixels (pixel size of 35 µm). For quantitative mineral-chemical points analyses, an accelerating voltage of 15 KeV and 50 nA of beam current was used. These were used as internal standards in the Q-XRMA tool (second cycle; Ortolano et al., 2018; Corti et al., 2019; Roda et al., 2021; Zucali et al., 2021; Caso, 2023) to obtain calibrated mineral maps showing the element content (expressed in atoms per formula unit; apfu) for selected mineral phases (biotite and garnet). By doing so, it was possible to highlight chemical variations and zoning within crystals within different microstructural sites and use them to better constrain the tectono-metamorphic evolution of the study area.

Insert Figure 4 here.

The tectono-metamorphic stages are named using a numerical progression (e.g., D_1, D_2, etc.). The prefix D- stands for deformation, S- indicates foliations, A- fold axes, F- for folds, and A.P.- stands for axial plane. Mineral formulae were calculated according to Deer et al. (1992) and using pyMinColab v.2023 (Zucali, 2023).

4. Rock types

The Valpelline Series is mostly made by metapelites, including migmatite gneiss and sillimanite-gneiss. Migmatite gneiss is the most common rock type and comprises both stromatic diatexites and

metatexites. Most migmatites are garnet-bearing, but in different localities of the valley cordierite–garnet-bearing migmatite gneiss also occurs (see yellow stars in Figure 2a; Gardien et al., 1994; Manzotti & Zucali, 2013; Caso, 2023; Caso et al., 2024). More rarely, garnet–orthopyroxene-bearing migmatite gneiss are also found (see red star in Figure 2a; Caso et al., 2024). Sillimanite-gneiss and minor felsic granulites occur as decametric to hectometric bodies interlayered with migmatite gneiss. Metabasic rocks correspond to basic granulites and brown amphibolites occurring in meter-sized lenses/boudins embedded in migmatite gneiss, and black amphibolite occurring as hectometric bodies interlayered with metapelites, and locally affected by partial melting. Marble and calcsilicatic rocks also crop out as hectometric bodies interlayered with metapelitic rocks and black amphibolites (Figure 2a; see Caso et al., 2024 for detailed lithological description).

In particular, in the Lac Mort area covered by LiDar and UAVs flights (Fig. 2a), two main groups of lithologies occur: (i) basic granulite and brown amphibolite and (ii) cordierite-bearing migmatite gneiss. In particular, the rocks of the former group crop out as meter-sized levels or boudins embedded in the cordierite-migmatite gneiss (not mappable at the map resolution scale; Fig. 2a) and locally folded.

Basic granulite shows a granoblastic to slightly gneissic fabric made by the isorientation of orthopyroxene and clinopyroxene and minor whitish plagioclase-rich aggregates. Brown amphibolite has a more pronounced gneissic structure made by the isorientation of brown amphibole and millimetric plagioclase. Cordierite-migmatite gneisses here mainly correspond to metatexites, showing a gneissic texture made by alternating leucosomes and melanosomes, which follows the regional foliation trend and lithological boundaries. The paleosome locally occurs as fine-grained pluridecimetric levels made of pyroxene, amphibole, biotite and plagioclase, similar to basic granulites. Melanosomes include millimetric isoriented biotite and minor millimetric fibrous sillimanite defining the main foliation. Leucosomes are made of fine-grained plagioclase, quartz and locally minor K-feldspar. They show variable thickness, from centimetric to pluricentimetric,

occurring as regular levels parallel to the main foliation, locally folded, or plurimetric pods with irregular shapes. Locally, a second generation of leucosome makes irregular patterns cross-cutting the main fabric (the main melanosome-leucosome alternation parallel to the regional foliation). Garnet occurs as millimetric to pluri-millimetric reddish porphyroblasts both in the melanosomes and leucosomes, together with cordierite. The latter constitutes dark-grey porphyroblasts from pluri-millimetric to centimetric. Within migmatites pluri-centimetric to metric lenses and boudins of fine-grained migmatitic gneiss also occur. They have a granoblastic structure made of plagioclase, quartz and minor garnet. Also, these portions, together with the migmatitic gneiss are cross-cut by centimeter-thick and discordant leucosomes.

As stated above, cordierite-migmatite gneisses were detected in several localities of the VP (see yellow stars in Fig. 2a). Nevertheless, it is hard to find fresh cordierite crystals within collected rock samples suitable for reliable microstructural investigation and mineral analysis at the EMPA. Indeed, most of the recognised cordierite blasts in thin sections are characterised by local or complete transformation into fine-grained white mica or chlorite aggregates (Fig. 5) during late retrogression (pinitisation; Schreyer and Seifert, 1970; Ogiermann and Kalt, 2000). The two selected samples analysed in this work have been chosen from the Comba Vessonaz area (red dots in Fig. 2a) since they show freshly preserved cordierite. Sample VP34 is representative of a melt-rich portion, while the 33SC shows a well-developed sillimanite-rich foliation suitable for microstructural constraints. Samples collected at the Lac Mort area (where the mesostructural study has been carried out) showed strongly retrogressed cordierite and were not homogeneous or suitable for the tectono-metamorphic reconstruction.

Insert Figure 5 here.

5. Results

5.1 Traditional mesostructural analysis

Together with field observations, (Fig. 6) a number of 154 orientations of structural elements has been derived from compass measurements (Fig. 7).

The S_1 foliation is the internal foliation of basic granulite and brown amphibolite boudins wrapped by the S_2, locally geometrically discordant to the long axis of the boudin and S_2 (Fig. 6a). In particular, at the mesoscale, S_1 has been detected in correspondence F_2 isoclinal folds, where this foliation is not completely transposed (Figs. 6b). In the basic granulite boudins, S_1 is a layering marked by the isorientation of pyroxene- and plagioclase-rich domains and by amphibole-rich and plagioclase-rich domains in the brown amphibolites. S_1 dips mainly toward NE, with variable but relatively high dip angles (Fig. 7a). The mean orientation from field data, calculated from the Kamb contouring is 164/55°.

S_2 foliation is penetrative in migmatite gneiss. It is defined by the alternation between melanosomes and leucosomes, and by the isorientation of biotite and sillimanite. S_2 dips mainly toward the S–SE with variable dip angles, which are locally sub-vertical. Locally it also dips toward the NW sub-vertically (Fig. 7c). The mean orientation calculated from the Kamb contouring field data is 142°/54° (dip direction and dip angles). A_2 axes, folding S_1, trend toward S–SW and plunge at 60–80°; A.P.$_2$ axial planes dip toward S–SE with almost sub-vertical dip angles (Fig. 7e). S_2 is widely deformed and folded by isoclinal (Fig. 6c, d) to open (Fig. 6e) F_3 folds, locally asymmetric, with a W-vergence (Figs. 6e). In correspondence with the isoclinal folds, S_2 and leucosomes are folded, and S_3 axial plane foliation locally develops (Fig. 6d). S_3 dips toward SE, with relatively high dip angles (Fig. 7g). Cordierite is also deformed in correspondence of fold hinges, here occurring as dark-grey aggregates (Fig. 6c). Locally, centimetric-thick leucosomes cross-cut S_2 foliation, along the limbs of F_3 folds (Fig. 6e). These leucosomes also cross-cut the basic granulite boudins, making “a-type” flanking structures with a top-to-the W sense of shear, with the leucosomes behaving as a cross-cutting element (CE; Hudleston, 1989; Mukherjee, 2014; Fig. 6f). The centimeter-thick leucosomes discordant to the S_2 dip toward E–SE and WSW (Fig. 7f). In some outcrops the F_3 folding produces a crenulation

cleavage S_3 (Fig. 6g). A_3 fold axes trend toward the S and plunge at 50–88°; $A.P._3$ axial planes dip toward the SE with dip angles ranging between ~45 and 75° (Fig. 7g). Kfs-Qz pegmatites and aplites, with different orientations and crosscutting relationship with the above-described structures, occur. The mineralogy between the different systems is the same. One system of dykes is parallel to the migmatitic foliation S_2 and is locally affected by boudinage (Fig. 6h); two late systems with different orientations cross-cut each other and the folded S_2 (Figs. 6h and i), striking NW–SE and NNW–SSE (Fig. 7h, i), both with dip angles ranging approximately from 65° to 85° (Fig. 7i). Moreover, some of these late dykes are also affected by open folds (Fig. 6h). Cross-cut relationships visible on the field highlight that aplites and pegmatites striking NW–SE (red dotted line in Fig. 6i) have been emplaced after those striking NNW–SSE (yellow dotted line in Fig. 6i).

Insert Figure 6 here.

5.1.2 3D virtual-outcrop analysis

A total number of 369 orientations have been extracted from remote sensing data (Fig. 7): in particular, 25 from UAV-derived point clouds, 107 from LiDAR-derived point clouds both processed in CloudCompare, and 209 from Google Satellite© using the *Qgsurf* plug-in within QGIS.

Insert Figure 7 here.

S_1 in basic granulite and brown amphibolite boudins has been traced and measured using the point clouds derived from iPad LiDAR scanning. 32 planes have been extracted (black dots in Fig. 7b). The extracted surfaces have a dip direction both toward S–SE and N–NE. The first extracted cluster has a dip direction ranging from ~150° to ~190° and dip angles between ~55° and 88°; the second one has a dip direction of ~350° or between ~5°–20° and two sub-clusters of dip angles, one more sub-vertical and one between ~40° and 65° (Fig. 7b). Planes extracted from the point clouds partially overlap those measured in the field: only the first cluster of orientations dipping toward S–SE is coherent with field measurements (green squares in Fig. 7a). The pervasive foliation S_2 at the outcrop

scale has been extracted both from the LiDAR point clouds and the UAV-derived one. The surfaces have a dip direction both toward NE and SE. The first denser cluster has dip directions ranging from ~145° to 195° and dip angles between 20° and 60°; the second one has dip directions between 315° and 360° and dip angles between 0° and 10°, with dip angles similar to the first cluster (Fig. 7d). S_2 orientations extracted from CloudCompare overlap only the cluster dipping toward the S. S_2 orientations extracted from UAV point cloud (black dots in Fig. 7d) partly overlap those from LiDAR and field, but are more scattered, and with relatively lower dip angles. Axes and axial planes related to the D_2 and D_3 folding have not been extracted from CloudCompare due to the relatively low resolution of the point clouds and the 3D outcrop flat shape not permitting line measurements of the axes. For leucosomes discordant to S_2, only strikes have been plotted since the low resolution of the point clouds and the size of the object, the dip angles were scattered or wrong (Fig. 7f).

29 data of aplites and pegmatites directions visible from both the UAV and LiDAR point clouds have been extracted. There are two main clusters of directions: (i) one strikes NW–SE and (ii) the second strikes WNW–ESE (Figs. 7j, k). Minor clusters striking E–W and NE–SW have also been measured from CloudCompare. The data extracted from the *Qgsurf* plug-in are more scattered and cover various orientation strikes: the most frequent is the one striking ENE–WSW (Fig. 7l). The data extracted from CloudCompare match better with those measured on the field with the compass.

5.2 Traditional microstructural analysis

Sample VP34 comes from a leucosome-rich portion. It is characterised by a gneissic structure mostly made by pluricentimetric-thick leucocratic levels consisting of plurimillimeter quartz, K-feldspar and cordierite and rare plagioclase alternating with few millimeter-thick sillimanite and biotite-rich melanocratic domains (Fig. 8a). Millimeter-sized garnet porphyroblasts mostly occur in melanosome and in minor amount in leucosome. Cordierite occurs within leucosomes as plurimillimeter-sized porphyroblasts (Fig. 8a). 33SC sample comes from a melanosome and differs from the former for the higher modal abundance of sillimanite, biotite and garnet. In this sample, the pervasive foliation is

made by millimeter-sized fibrous and prismatic sillimanite with minor biotite and ilmenite (Figs. 8b and c). Leucosomes are thin, discontinuous and composed of millimeter-sized quartz and minor plagioclase, without K-feldspar (Fig. 8c). Garnet occurs as plurimillimeter-sized and locally flattened porphyroblasts wrapped by the main foliation. In this sample cordierite is mosly plurimillimeter-sized, strongly fractured and locally pseudomorphed by fine white mica aggregates (Fig. 8c).

Insert Figure 8 here.

S_2 is marked by the SPO of sillimanite (Sil II), biotite (Bt II; Figs. 9a and 10) and ilmenite, alternating with leucosomes, made of quartz (Qz II), K-feldpsar and plagioclase in sample VP34 (Fig. 9b). Locally, minor deformations in Bt II crystals along S_2 are observed. Quartz grain size is variable, from plurimillimeter ribbons to millimeter and sub-millimeter equant blasts. Coarse-grained quartz ribbons are oriented marking the S_2 fabric (Fig. 9b). Plagioclase occurs as rare millimeter blasts in the leucosomes of sample VP34 and in discontinuous millimeter-thin levels in sample 33SC, together with quartz. S_2 in sample 33SC is preserved as fold hinges within microlithons of the locally spaced S_3 (Figs. 9c, d). S_3 is well developed in this sample and is marked by sillimanite (Sil III), idiomorphic biotite lamellae (Bt III) and ilmenite, wrapping both garnet and cordierite porphyroblasts (Figs. 9d, e). Garnet in both samples hosts sub-millimeter inclusions of biotite (Bt I), sillimanite (Sil I), and quartz blasts (Qz I), having a rounded shape, thus not in equilibrium with garnet (Figs. 9c, d, f). Locally, sillimanite inclusions align in the rim of the garnet making an internal foliation in continuity with the external S_3 (Fig. 9f). Thus, garnet in sample 33SC grew from pre- to syn-kinematic (Passchier and Trouw, 2005) with respect to S_3. Some of these syn-kinematic garnet porphyroblasts also have a flattened shape (Figs. 8b, c and 9f). Fine-grained aggregates of white mica locally overgrow both cordierite and K-feldspar. Quartz and biotite along S_3 foliation locally make intergrowths after garnet (Qz III and Bt III).

Insert Figure 9 here.

Insert Figure 10 here.

395 *5.2.1 Quantitative microstructural analysis*

396 The Mineral-Grain-Size detector tool (Min-GSD) applied to both samples provided two vectorial
397 grain polygon maps whose grains are labelled with a mineral phase attribute (Figs. 11a and b). As a
398 result, the following rock-forming mineral grains have been distinguished in samples VP34 and 33SC
399 respectively: 1,125 and 15,058 sillimanite grains, 1,275 and 4,049 biotite grains, 112 and 1,277 garnet
400 grains, 2,092 and 757 white mica grains, 560 and 432 cordierite grains, 1,086 and 397 plagioclase
401 grains, 86 and 384 ilmenite grains, 1,929 and 311 quartz grains; in sample 33SC 127 chlorite grains
402 and 11 rutile grains occur. K-feldspar, detected only in sample VP34, has a number of 2,509 grains
403 (Fig. 11a). These values result in different modal percentages, obtained from the Q-XRMA first cycle
404 classification, highlighting huge differences mineral modes (Fig. 11c). Quartz + feldspars
405 (corresponding to leucosome) grains percentage differs in the two samples: in sample VP34 this sum
406 (quartz + K-feldspar + plagioclase) is relatively high (~70%) corresponding to 5,524 grains (yellow
407 grains in the right of Figure 11a); in sample 33SC quartz + plagioclase sum is much lower,
408 corresponding only to ~5% vol with 708 total grains (yellow grains in the bottom of Figure 11b).
409 Accordingly, biotite + sillimanite grains percentage (corresponding to the melanosome) is higher in
410 sample 33SC (~70%) and lower in VP34 (~10%). The same is for garnet which is more abundant in
411 sample 33SC (Fig. 11c).

412 *Insert Figure 11 here.*

413 Grain orientations data have been extracted from each mineral phase to check whether a link between
414 their orientations and the foliation they mark occurs. In particular, the MFA calculates the long axis
415 orientation angle (0–180°) measured clockwise from a reference vertical axis. The long axis
416 orientation values are clustered at ~ 90° for biotite, sillimanite, ilmenite and quartz (Fig. 12a). In
417 detail, biotite, sillimanite and ilmenite long axis orientations mostly have values of ~90°, with two
418 minor clusters at ~ 60° and ~120° for both samples. In sample VP34, all phases also show a
419 pronounced cluster between 60° and 90°, reflecting the local anastomosed geometry of S_2 foliation.

There is a relatively small number of grains with long axis orientation at 0° or 180°, and these occurrences are more common in the sample 33SC. Garnet orientations have been plotted only for sample 33SC, where, despite exhibiting more dispersion compared to other mineral phases, they show a weak clustering of orientations at ~ 90° (Fig. 12a). Similarly, this pattern emerges for K-feldspar found exclusively in sample VP34, where a slight clustering around 90° is observed (Fig. 12a).

The long axis orientation data is easily observed through orientation maps extracted from ArcGIS (Figs. 12b, c, d, e, f, g). S_2 in sample VP34 is defined by the sillimanite and biotite grains whose long axes have orientations between ~60° and 110° (Figs. 12b and c). Quartz and K-feldspar long axis orientations in the leucosome, with angles comprised between ~60° and 110° (light blue and yellowish shades; Figs. 12d and e), also support S_2.

Looking at sillimanite long axis orientation maps for sample 33SC (as already shown in Caso, 2023), the grains having orientation at ~ 90° are those marking the main S_3 foliation (Figs. 12f, g). Grains having various orientations, such as 0–30° (light-blue shades) or 130–180° (reddish shades; Figs. 12f and g) mark S_2 in the microlithons (see zoom rose diagram and map in Fig. 12g). Also, some of more scattered orientations not directly correlated with S_2 may be represented by grains included within garnet.

Insert Figure 12 here.

Quartz and K-feldspars grains locally show SPO in sample VP34, marking S_2 foliation. This is constrained through the roundness parameter (calculated as the width/lenght ratio of each grain) of these two mineral phases (Figs. 13a, b). Quartz marking S_2 corresponds to grains with roundness between 0.19 and 0.53 (yellow-orange grains in Fig. 13a). Purple and blue grains correspond to those whose roundness is closer to 1 and are not suitable for marking S_2 (Figs. 13b and c). As shown in the rose diagram for sample 33SC, a huge number of garnet grains has long axis with orientation at ~ 90° (Fig. 12a), parallel to the main S_3 foliation (yellow, green, and orange grains in Fig. 13d). In this case, the roundness parameter of garnet is often lower than 1 (yellow to orange grains; Figs. 13e, f). This

445 is in accordance with the flattened shape of the grains, making them suitable for marking S_3 foliation
446 (Figs. 13e, f).

447 *Insert Figure 13 here*

448 **6. Quantitative mineral-chemical analysis**

449 Mineral-chemical analysis on sample 33SC was carried out on biotite and garnet by Caso (2023)
450 using a different software. Here we used the Q-XRMA second cycle to obtain biotite and garnet-
451 calibrated maps, extending the comparison with EMPA point analyses and deeply discussing the
452 results.

453 Mg, Fe and Ti calibrated maps were analysed to check biotite chemical variations. The Mg content
454 in biotite varies from 2.39 to 3.24 apfu (Fig. 14a). Fe varies from 1.50 to 2.20 apfu (Fig. 14b), resulting
455 in Mg# (Mg/Fe+Mg) from ~0.5 to 0.7 (Fig. 14c). Mg increases toward the core and is higher in the
456 biotite grains in the garnet strain shadows (Fig. 14a). Conversely, Fe is higher in biotite grains
457 included within garnet porphyroblasts, at the rim of the grains marking the S_3 foliation and in biotites
458 replacing cordierite (Fig. 14b). The Ti content ranges from 0.30 to 0.70 apfu (Fig. 14d) and is higher
459 in biotite grains included within garnet (Bt I) and increases in the core of some coarser biotite blasts
460 (Bt II). The lowest values are found in some biotites marking the main S_3 foliation (Bt III), especially
461 in those growing after cordierite (Fig. 14d).

462 The Ti content of biotite has been used for calculating the temperatures through the Ti-in-biotite
463 thermometer of Henry et al. (2005). Considering only EMPA point mineral-chemical data (pink
464 symbols in Fig. 14c), the *T* ranges between 730 and 800°C; using Ti content extracted from each pixel
465 of the calibrated map, the *T* range becomes wider, with a mean cluster between 650 and 800°C.

466 Garnet has already described in Caso (2023) and is mostly homogeneous. It shows only a weak
467 zonation for Ca, thus with increasing grossular component toward the rim. Mg and Fe apfu, as visible
468 from calibrated maps, are homogeneous with a slight variation toward the rim, especially when in

contact with biotite (Figs. 14e, f). Mg is mostly between 0.77–0.80 apfu, up to decreasing at 0.69 in the rim in contact with biotite (Fig. 14e). Fe is homogeneous in most of the blasts, being 2.13 apfu, up to 2.22 in the rim in contact with biotite (Fig. 14f). All chemical data obtained by the EMPA and extracted from each pixel of the calibrated maps are reported in Supplementary Material 2.

Insert Figure 14 here.

7. Discussions

7.1 Tectono-metamorphic evolution of the Valpelline Series

The multiscale and multi-method structural analysis allowed the definition of three tectono-metamorphic stages in the Valpelline Series, namely D_1, D_2 and D_3 (Fig. 15).

D_1 is testified by the S_1 foliation, preserved mostly in basic granulite and brown amphibolite boudins and locally discordant to the external S_2 (Figs. 6a, b and 15). S_1 dips mainly toward the SW with scattered dip angles. At the microscale, in metabasic rocks, this foliation is defined by the alignment of clino- and orthopyroxene, brown amphibole, plagioclase and in minor amounts biotite and orthoamphibole (see Caso et al., 2024 for details about D_1). In migmatite gneiss is harder to constrain the D_1: the round-shaped inclusions of Bt I, Sil I, and Qz I within garnet or cordierite may be both remnants of the D_1 stage in the hosting migmatitic gneiss or just inclusions from the D_2 stage.

Extracted quantitative parameters for the rock-forming mineral phases support the above-described relationships: part of biotite, sillimanite and quartz grains with long-axis orientations diverging from the main foliation (Fig. 12a) can be ascribed to Bt I, Sil I and Qz I grains included within garnet and cordierite which show no preferred orientation. Nevertheless, this parameter alone is not sufficient for this constrain; most of these grains have a round shape, rarely elongated, corresponding to grains with roundness (w/l) parameter closer to 1 (e.g., quartz data in purple and blue in Figures 13c). Mineral-chemical variations are not strongly enough to constrain these relationships, since H*T* metamorphism often led to chemical homogenisation during cooling. However, only Bt I included

493 within garnet locally preserve chemical variation, thus being characterised by the highest Ti values
494 (0.5–0.7 apfu; Figs. 14c and d), resulting in higher calculated temperature up to ~800 °C (Fig. 14d).

495 During this stage S_1 is deformed and S_2 axial plane foliation develops. S_2 is characterized by the
496 alternation between melanosomes and leucosomes within migmatite gneisses. S_2 dips toward the SW,
497 with high dip angles. At the microscale, S_2 is well-developed in sample VP34 and is highlighted by
498 SPO of sillimanite and biotite (Sil II and Bt II) in the melanosomes and SPO of quartz (Qz II) and K-
499 feldspar in the leucosomes. Quartz grains highlighting S_2 in sample VP34 (Qz II) are those having a
500 relatively low roundness parameter, due to their elongated shape (Figs. 13a, c). The long axis
501 orientations with a main cluster oriented at ~90°, extracted through the MFA tool for these mineral
502 phases highlight S_2. Long axis orientations at 30° and 120° support the presence of Bt II highlighting
503 the remnants of the S_2 within the microlithons of sample 33SC. Locally within these domains, larger
504 deformed Bt II grains show a relatively high-Ti content (~0.5 to 0.7 apfu; Figs. 14c and d).

505 Leucosome percentage (quartz + plagioclase + K-feldspar), estimated at the microscale through the
506 MFA, may give an idea of the amount of melt present within the studied rock volume, in this case
507 higher in sample VP34 (Fig. 11a). However, leucosome does not always represent the melt-fraction
508 (e.g., Lee et al., 2020) or it can easily escape during brittle or shear deformation (Sawyer, 2001;
509 Etheridge et al., 2021; Daczko & Piazolo, 2022). Moreover, it can also be possible that some of the
510 K-feldspar or plagioclase blasts occurring within leucosomes represent solid peritectic products of
511 biotite-dehydration melting reaction (Le Breton & Thompson, 1981; Spear, 1994; Waters, 2001;
512 White et al., 2014) and not always something crystallised directly from the melt. Nevertheless, in
513 these samples and in others of the VP, several melt-bearing microstructures have been recognised
514 (Caso et al., 2024), such as melt films among grain boundaries or back-reaction structures after melt
515 consumption (e.g., biotite-quartz intergrowths; Sawyer, 2008; Kreigsman & Alvarez-Valero, 2010),
516 related to the D_2-D_3 stages. It is harder to estimate how much melt has been produced in sample 33SC:
517 this may represent a situation where most of melt has escaped from the rock volume or has been

consumed during back-reaction involving peritectic phases and melt, producing biotite and sillimanite.

Garnet and cordierite, which occur within leucosomes formed during D_2, represent peritectic phases, according to the Bt + Sil + Qz + Pl = Grt + Crd + Kfs + melt reaction (Kreigsman and Alvarez-Valero, 2010; Waters, 2001; White et al., 2014). The mutual relationship between garnet and cordierite is not easy to constrain; however, both are wrapped by S_3 sillimanite-biotite foliation, constraining their growth during the D_2 (see also Caso et al., 2024).

Garnet growth relations during the partial melting evolution are difficult to reconstruct using mineral-chemical criteria; these are homogenous and show almost no chemical zoning, apart from weak zoning of Fe and Mg toward the edge in contact with biotite, due to late diffusional resetting during cooling. This is also testified by temperatures obtained in these rocks using the Grt-Bt exchange thermometer: temperatures go down to 650°C (Caso et al., 2024).

During D_3, S_2 is deformed with open to isoclinal folds, with the local development of the sillimanite-rich S_3 foliation (Figs. 6c, d, e, f and 15). During this stage, leucosomes and cordierite are deformed. This is more evident at the mesoscale, where dark-grey aggregates of cordierite are folded and concentrated in the fold hinges (Figs. 6d and 15).

At the microscale, S_3 is well observable in sample 33SC and it is marked by the SPO of sillimanite and biotite. The long axis orientations with a main cluster oriented at ~90°, extracted from MFA tool for sillimanite, biotite, and ilmenite refer to S_3 (i.e., Sil III and Bt III). Even though garnet grows during D_2 it continues its crystallisation during the early D_3. Quantitative MFA data of garnet demonstrate the presence of flattened porphyroblasts corresponding to those having a roundness locally strongly < 1 (Fig. 13e, f). Bt III corresponds to grains having a lower Ti content with respect to Bt I and Bt II, ranging from ~0.3 to 0.5 apfu and thus yielding slightly lower temperatures between ~650–730 °C (Fig. 14d).

The two analysed samples are representative of different stages of the partial melting history of the VP: indeed, sample VP34, which corresponds to a cordierite-bearing leucosome (Fig. 12a), is representative of melt production during D_2, since its main foliation corresponds to S_2. Conversely, sample 33SC is almost devoid of leucosomes, apart from rare millimeter-thin levels, and is strongly enriched in sillimanite and biotite that mark S_3 foliation, with S_2 preserved in few microdomains as relict fold hinges. Thus, this sample may represent the melt-consuming reactions during D_3, where such a high modal amount of sillimanite can be produced by garnet or cordierite back-reacting with melt, giving Sil III and Bt III (Spear, 1994; Kreigsman and Alvarez-Valero, 2010). Meanwhile, is also possible that part of melt has escaped from this rock during D_3, migrating toward low-strain zones where the S_2 fabric is well-recognisable.

Geometrical overprinting relationships between different systems of aplite and pegmatite dykes, which widely intrude into the migmatr gneiss, allowed to divide the D_3 into an early and late D_3 stage (Fig. 15). One system of dykes parallel to the S_2 and locally affected by boudinage (Fig. 6h) may have intruded gneiss during the D_2 or early D_3 stage. Then, other systems of dykes intruded migmatites by cross-cutting the syn-D_2 and syn-D_3 foliations and folds (Figs. 6h, i). Moreover, part of these dykes cross-cutting D_3 folds, and striking NNW-SSE are also locally affected by open folds (Fig. 6h), probably developed during the ongoing deformation during early D_3 (Fig. 15). It is possible that dykes started intruding migmatites during late stages of D_2, using the S_2 foliation as preferential path or weakness layer, being progressively affected by boudinage during progressive deformation; then, during D_3 folding, some intruding dykes are folded. In the latest stages of D_3, dykes intruded migmatite gneiss, crosscutting all structures (D_2 + D_3) without being further deformed.

Insert Figure 15 here.

7.2 Pros and cons of quantitative multiscale structural analysis

565 The multiscale digital acquisition methods used in this work have given an interdependent picture of
566 the reconstructed sequence of deformation events (Fig. 15). This allowed also to better constrain the
567 paragenetic sequence on which the thermodynamic calculations are usually based (Palin et al., 2016).

568 In particular, the quantitative mesoscale structural analysis made by the integration of traditional
569 compass measurements with data extracted from LiDAR sensor or UAVs-derived point clouds,
570 allowed to collect a statistically high number of structural data (in most cases more than ~50), even
571 from inaccessible outcrop portions. Nevertheless, there are still some structural artefacts resulting
572 from the use of CloudCompare on point clouds. In this case, the problems were eliminated by the
573 direct ground control carried out during the traditional survey campaign (i.e., comparison with
574 compass manual measurements of structural elements). Indeed, even though most of the S_1 and S_2
575 data extracted from CloudCompare fit well with the ones measured on the field (see Figs. 7a, b, c, d,
576 b), this software often extracts orientations having the same strike as those measured with the
577 compass, but with opposite dip directions. This can be explained by a difference in the dip angle of a
578 few degrees (5–10°) which apparently changes the dip direction of sub-vertical planes. However, this
579 misfit may derive from systematic errors during field-based data collecting, especially of sub-vertical
580 planes where the user is often led to make the planes dip toward the same direction. Moreover, as is
581 often the case, these artefacts can be also caused by: a) the low density of the point clouds useful for
582 reconstructing the 3D model; b) the presence of shadows during LiDAR or UAVs acquisitions; c)
583 flattened outcrop exposure leading to wrong plane interpolation and measure; d) the difficulty of
584 acquiring data in places that are too inaccessible leading to a low number of data to be used as ground
585 control. Although the technique still has some problems to overcome, it should be able to integrate
586 perfectly with the traditional methods used to date. Data extracted measuring the orientations of dykes
587 polylines traced on Google Satellite© in QGIS, are the most scattered. This dispersion probably
588 derived from artefacts and "holes" of the DEM itself, used by the *Qgsurf* plug-in to measure dip
589 directions and dip of a plane interpolated from the traced polyline. This problem should be overcome

590 in two ways: (i) using a higher resolution DEM, better though extracted from UAVs survey which
591 can have resolutions of few centimeters; (ii) by carefully excluding, using manual data as ground
592 control, orientations without a geological meaning. Nevertheless, this technique has the advantage of
593 being low-cost, since Google Satellite© and QGIS tools are freely available and do not require
594 expensive hardware to be used.

595 On the other hand, also conventional structural analysis, characterised by the manual collection of
596 structural data, is a process which may be susceptible to human errors and biases. Therefore, to obtain
597 an objective structural assessment, the integration of traditional methods and semi-automated
598 techniques is necessary to have a double-check of structural measurements and quantitively constrain
599 the polyphase deformation.

600 The possibility of storing vectorised, microstructure-derived large datasets subdivided by mineral
601 phase through the MFA toolbox, opens up the possibility of following the path of a true digital
602 transition of geo-petrostructural data system acquisition, possibly within a unique and interoperable
603 geological large data system (georeferenced GIS databases). However, these data may still be
604 somewhat cumbersome to obtain since it is necessary to acquire EMPA X-ray maps with adequate
605 resolution, resulting in high costs and time-consuming grain post-processing.

606 Nevertheless, these digital storing of microstructural data will open the possibility of better
607 interoperate with previously available datasets, allowing them to be integrated synergistically in a
608 broader sense.

609 ## 8. Conclusions

610 This work described a multiscale approach that combines traditional field-based methods with
611 remote-sensing and quantitative techniques useful to investigate crystalline basements. In particular,
612 we have integrated traditional structural survey with the extraction of structural data from LiDAR
613 and UAVs-derived point clouds, and Google Satellite©. Using the point clouds and Google Satellite©

614 imagery, we extracted structural data also from steep inaccessible outcrop portions, extending the
615 observation scale. This allowed for increasing the number of the main structural element orientations
616 (foliations, leucosomes and dykes), using the manual field compass data as ground control.
617 Traditional microstructural analysis was combined with the extraction of quantitative shape
618 parameters from semi-automated grain digitisation, stored in a GIS database, allowing to constrain
619 the structural evolution.

620 The provided quantitative multiscale structural analysis allowed the reconstruction of the tectono-
621 metamorphic evolution of the migmatitic rocks in the Valpelline Series. In particular, three main
622 tectono-metamorphic stages have been recognised, referred to the H*T* evolution of the VP crust during
623 the Permian. D_1 is a solid-state tectono-metamorphic stage, testified by the S_1 foliation preserved in
624 basic granulite and brown amphibolite boudins. D_2 is related to melt production and development of
625 the regional S_2 foliation, garnet, and cordierite growth; early D_3 is characterised by folding of the S_2
626 and local development of S_3 sillimanite-rich melt-consuming foliation wrapping around garnet and
627 cordierite porphyroblasts. Lastly, three systems of aplites and pegmatites intrude within migmatitic
628 gneiss from early- to late D_3-stages, cross-cutting all the migmatitic structures.

629 The integration of traditional and innovative multiscale structural analysis has proven to be an
630 efficient approach to ease the study of migmatitic crystalline basements, characterised by complex
631 superimposed structures and different metamorphic assemblages.

632 **Acknowledgements**

633 We thank two anonimous reviewers the editor F. Agosta for their useful suggestions. This research
634 has been funded by "PSR2020_MRODA". The results here presented have been developed in the
635 frame of the MIUR Project "Dipartimenti di Eccellenza 2017—Le Geoscienze per la società: risorse
636 e loro evoluzione (work package 3, tasks 3.3 and 3.4)". The work was partly supported by the Italian
637 Ministry for Universities and Research (MUR) through the project "Dipartimenti di Eccellenza 2023-
638 27".

References

Allmendinger, R.W., Cardozo, N.C., Fisher, D., 2013. Structural Geology Algorithms: Vectors & Tensors. Cambridge University Press, Cambridge, England.

Angiboust, S., Glodny, J., Oncken, O., Chopin, C., 2014. In search of transient subduction interfaces in the Dent Blanche–Sesia Tectonic System (W. Alps). Lithos 205, 298–321. https://doi.org/10.1016/j.lithos.2014.07.001

Angrand, P., Mouthereau, F., 2021. Evolution of the Alpine orogenic belts in the Western Mediterranean region as resolved by the kinematics of the Europe-Africa diffuse plate boundary. BSGF-Earth Sciences Bulletin 192(1), 42. https://doi.org/10.1051/bsgf/2021031

Ashworth, J.R., 1985. Migmatites. Glasgow and London (Blackie & Son Limited).

Beltrando, M., Compagnoni, R., Lombardo, B., 2010. (Ultra-) High-pressure metamorphism and orogenesis: An Alpine perspective. Gondwana Res. 18, 147–166. https://doi.org/10.1016/j.gr.2010.01.009

Bonasera, M., Cerrone, C., Caso, F., Lanza, S., Fubelli, G., Randazzo, G., 2022. Geomorphological and Structural Assessment of the Coastal Area of Capo Faro Promontory, NE Salina (Aeolian Islands, Italy). Land 1(7), 1106. https://doi.org/10.3390/land11071106

Bonasera, M., Petroccia, A., Caso, F., Cerrone, C., Gregorio, F., 2023. Integrated geomorphological and structural analysis of coastal cliffs: The case study of Capo Faro Promontory, NE Salina, Aeolian Islands, Italy. 2023 IEEE International Workshop on Metrology for the Sea; Learning to Measure Sea Health Parameters, MetroSea 2023 - Proceedings, 2023, 519–523. https://doi.org/10.1109/MetroSea58055.2023.10317191

Brandolini, F., Cremaschi, M., Zerboni, A., Degli Esposti, M., Mariani, G.S., Lischi, S., 2020. SfM-photogrammetry for fast recording of archaeological features in remote areas, in: Bagnasco G.,

662 Bortolotto S., Garzulino A., Marzullo M. (Eds.), Milano internazionale: la fragilità territoriale dei
663 contesti archeologici. Atti del Convegno Internazionale (Milano, 13 marzo 2019), «Archeologia e
664 Calcolatori», 31.2, 33–45. https://doi.org/10.19282/ac.31.2.2020.04

665 Brown, M., 1973. The definition of metatexis, diatexis and migmatite. Proceedings of the Geologists'
666 Association 84, 371–382. https://doi.org/10.1016/S0016-7878(73)80021-5

667 Cardozo, N., Allmendinger, R.W., 2013. Spherical projections with OSXStereonet. Comput. Geosci.
668 51, 193–205. https://doi.org/10.1016/j.cageo.2012.07.021

669 Caso, F., 2023. Quantitative combined multiscale structural and minero-chemical analysis to unravel
670 the tectono-metamorphic evolution of cordierite-migmatite gneiss from the Valpelline Unit (Dent-
671 Blanche Nappe, Western Italian Alps, Valle d'Aosta). Rend. Online Soc. Geol. It. 60, 2–10.
672 https://doi.org/10.3301/ROL.2023.20

673 Caso, F., Strambini, A., Zucali, M., 2024. Structural, lithostratigraphic and thermal features of a
674 Permian lower crust from the Western Italian Alps (Valpelline Series, Valle d'Aosta). Geological
675 Magazine, *in press*. https://doi.org/10.1017/S0016756824000037

676 Cawood, A.J., Bond, C.E., Howell, J.A., Butler, R.W.H., Totake, Y., 2017. LiDAR, UAV or
677 compass-clinometer? Accuracy, coverage and the effects on structural models. J. Struct. Geol. 98,
678 67–82. http://dx.doi.org/10.1016/j.jsg.2017.04.004

679 Corti, L., Zucali, M., Visalli, R., Mancini, L., Mohammad, S., 2019 Integrating X-ray computed
680 tomography with chemical imaging to quantify mineral re-crystallization from granulite to eclogite
681 metamorphism in the Western Italian Alps (Sesia-Lanzo Zone). Front. Earth. Sci. 7, 327.
682 https://doi.org/10.3389/feart .2019.00327

683 Dal Piaz, G.V., Bistacchi, A., Gianotti, F., Monopoi, B., Passeri, L., Schivo, A., 2016. Note
684 illustrative del F. 070 Monte Cervino della Carta geologica d'Italia alla scala 1:50.000. Memorie
685 Descrittive Carta Geologica D'Italia 101, 5–258.

686 Daczko, N.R., Piazolo, S., 2022. Recognition of melferite – A rock formed in *syn*-deformational high-
687 strain melt-transfer zones through sub-solidus rocks: A review and synthesis of microstructural
688 criteria. Lithos, 430–431,106850, https://doi.org/10.1016/j.lithos.2022.106850

689 Deer, W.A., Howie, R.A., Zussman, J., 1992. An introduction to the rock-forming minerals. John
690 Wiley and Sons, New York.

691 Dewey, J.F., Helman, M.L., Turco, E., Hutton, D.H.W., Knott, S.D., 1989. Kinematics of the western
692 Mediterranean, in: Coward, M.P., Dietrich, D., and Park, R.G., (Eds.), Alpine Tectonics, Geological
693 Society of London Special Publication 45, 265–283. https://doi.org/10.1144/GSL.SP.1989.045.01.15

694 Diehl, E.A., Masson, R., Stutz, A.H., 1952. Contributo alla conoscenza del ricoprimento della Dent
695 Blanche. Memorie degli Istituti di Geologia e Mineralogia dell'Università di Padova, 17, 1–52.

696 Etheridge, M.A., Daczko, N. R., Chapman, T., & Stuart, C. A. 2021. Mechanisms of melt extraction
697 during lower crustal partial melting. J. Metam. Geol. 39(1), 57–75,
698 https://doi.org/10.1111/jmg.12561

699 Fazio, E., Alsop, G.I., Nania, L., Graziani, R., Iaccarino, S., Montomoli, C., Carosi, R., Luzin, V.,
700 Salvemini, F., Gambino, S., Cirrincione, R., Mamtani, M.A., 2024. CPO and quantitative textural
701 analyses within sheath folds. J. Struct. Geol. 178, 105000. https://doi.org/10.1016/j.jsg.2023.105000ù

702 Gardien, V., Reusser, E., Marquer, D., 1994. Pre-Alpine metamorphic evolution of the gneisses from
703 the Valpelline Series (Western Alps, Italy). Schweizerische Mineralogische und Petrographische
704 Mitteilungen 74, 489–502.

705 Gosso, G., Rebay, G., Roda, M., Spalla, M. I., Tarallo, M., Zanoni, D., Zucali, M., 2015. Taking
706 advantage of petrostructural heterogeneities in subduction collisional orogens, and effect on the scale
707 of analysis. Per. Mineral. 84(3), 779–825. https://doi.org/10.2451/2015PM0452

Grasemann, B., Stüwe, K., Vannay, J-C., 2003. Sense and non-sense of shear in flanking structures. J. Struct. Geol. 25, 19–34. https://doi.org/10.1016/S0191-8141(02)00012-3

Handy, M.R., Schmid, S.M., Bousquet, R., Kissling, E., Bernoulli, D., 2010. Reconciling plate-tectonic reconstructions of Alpine Tethys with the geological- geophysical record of spreading and subduction in the Alps. Eart Sci. Rev. 102, 121–158. https://doi.org/10.1016/j.earscirev.2010.06.002

Heilbronner, R., 2011. Distortion of orientation data introduced by digitizing procedures. J. Microsc. 149(2), 83–96. http://dx.doi.org/10.1111/j.1365-2818.1988.tb04566.x

Heilbronner, R., Barrett, S., 2014. Image Analysis in Earth Sciences. Springer Berlin, Heidelberg. https://doi.org/10.1007/978-3-642-10343-8

Henry, B., Guidotti, C.V., Thomson, J.A., 2005. The Ti-saturation surface for low-to-medium pressure metapelitic biotite: implications for geothermometry and Ti-substitution mechanisms. Am. Mineral. 90, 316–28. https://doi.org/10.2138/am.2005.1498

Hopgood A.M. 1979. Polyphase fold analysis as a means of interpreting the deformational history of migmatites. Geology 31, 109–110.

Hudleston, P.J., 1989. The association of folds and veins in shear zones. J. Struct. Geol. 11(8), 949–957. https://doi.org/10.1016/0191-8141(89)90046-1

Johnson, S.E., Vernon, R.H., 1995. Inferring the timing of porphyroblast growth in the absence of continuity between inclusion trails and matrix foliations: can it be reliably done? J. Struct. Geol. 17(8), 1203–1206. https://doi.org/10.1016/0191-8141(95)00021-5

Kriegsman, L.M., 2001. Partial melting, partial melt extraction and partial back reaction in anatectic migmatites. Lithos 56(1), 75–96. https://doi.org/10.1016/S0024-4937(00)00060-8

Kriegsman, L.M., Alvarez-Valero, A.M., 2010. Meltproducing versus melt-consuming reactions in pelitic xenoliths and migmatites. Lithos 116, 310–320, https://doi.org/10.1016/j.lithos.2009.09.001

731 Kunz, B.E., Manzotti, P., von Niederhäusern, B., Engi, M., Darling, J.R., Giuntoli, F. Lanari, P.,
732 2018. Permian high-temperature metamorphism in the Western Alps (NW Italy). Int. J. Earth Sci.
733 107, 203–229. https://doi.org/10.1007/s00531-017-1485-6

734 Lanari P., Vidal O., De Andrade V., Dubacq B., Lewin E., Grosch E.G., Schwartz S., 2014.
735 XMapTools: a MATLAB©-based program for electron microprobe X-ray image processing and
736 geothermobarometry. Comp. Geosci. 62, 227–240. https://doi.org/10.1016/j.cageo.2013.08.010

737 Lardeaux, J.M., 2014. Deciphering orogeny: a metamorphic perspective. Examples from European
738 Alpine and Variscan belts: Part I: Alpine metamorphism in the western Alps. A review. Bulletin de
739 la Société Géologique de France 185(2), 93–114. https://doi.org/10.2113/gssgfbull.185.2.93

740 Le Breton, N.L., Thompson, A.B., 1988. Fluid-absent (dehydration) melting of biotite in metapelites
741 in the early stages of crustal anatexis. Contribution to Mineralogy and Petrology 99, 226–237,
742 https://doi.org/10.1007/BF00371463

743 Lee, S., Suh, J., Park, H-d., 2013. Smart Compass-Clinometer: A smartphone application for easy
744 and rapid geological site investigation. Comp. Geosci. 61, 32–42.
745 http://dx.doi.org/10.1016/j.cageo.2013.07.014

746 Lee, A.L., Lloyd, G.E., Torvela, T., Walker, A.M., 2020. Evolution of a shear zone before, during
747 and after melting. J. Geol. Soc. 177(4), 738–751. https://doi.org/10.1144/jgs2019-114

748 Manzotti, P., Zucali, M., 2013. The pre-Alpine tectonic history of the Austroalpine continental
749 basement in the Valpelline unit (Western Italian Alps). Geol. Mag. 150, 153–172.
750 https://doi.org/10.1017/S0016756812000441

751 Manzotti, P., Ballèvre, M., 2017. Tectonic history of the Dent Blanche. Geological Field Trips and
752 Maps 9(2.1), 73 pp. https://doi.org/10.3301/GFT.2017.02

753 Manzotti, P., Ballèvre, M., Zucali, M., Robyr, M., Engi, M., 2014a. The tectonometamorphic
754 evolution of the Sesia–Dent Blanche nappes (internal Western Alps): review and synthesis. Swiss J.
755 Geosci. 107(2), 309–336. https://doi.org/10.1007/s00015-014-0172-x

756 Manzotti, P., Zucali, M., Ballèvre, M., Robyr, M., Engi, M., 2014b. Geometry and kinematics of the
757 Roisan-Cignana Shear Zone, and the orogenic evolution of the Dent Blanche Tectonic System
758 (Western Alps). Swiss J. Geosci. 107,23–47. https://doi.org/10.1007/s00015-014-0157-9

759 Manzotti, P., Ballèvre, M., Pitra, P., Benita Putlitz, P., Robyr, M., Müntener, O., 2020. The Growth
760 of Sodic Amphibole at the Greenschist- to Blueschist-facies Transition (Dent Blanche, Western
761 Alps): Bulk-rock Chemical Control and Thermodynamic Modelling. J. Petrol. 61(4).
762 https://doi.org/10.1093/petrology/egaa044

763 Mattéo, L., Manighetti, I., Tarabalka, Y., Gaucel, J.-M., van den Ende, M., Mercier, A., Tasar, O.,
764 Girard, N., Leclerc, F., Giampetro, T., Dominguez, S., Malavielle, J., 2021. Automatic fault mapping
765 in remote optical images and topographic data with deep learning. Journal of Geophysical Research:
766 Solid Earth 126, e2020JB021269. https://doi.org/10.1029/2020JB021269

767 Midland Valley, 2015. FieldMove User Guide.

768 Misra, A.A., Mukherjee, S., 2023. Atlas of Structural Geological and Geomorphological
769 Interpretation of Remote Sensing Images. Wiley and Sons.
770 https://onlinelibrary.wiley.com/doi/book/10.1002/9781119813392.7

771 Mukherjee, S., 2014. Review of the flanking structures in meso- and micro-scales. Geol. Mag. 151,
772 957–974. https://doi.org/10.1017/S0016756813001088

773 Nicot, E., 1977. Les roches meso et catazonales de la Valpelline (nappe de la Dent Blanche, Alpes
774 italiennes). PhD Thesis, Paris.

775 Niedzielski, T., 2018. Applications of unmanned aerial vehicles in geosciences: introduction. Pure
776 and Applied Geophysics 175, 3141–3144. https://doi.org/10.1007/s00024-018-1992-9

777 Novakova, L., Pavlis, T.L., 2017. Assessment of the precision of smart phones and tablets for
778 measurement of planar orientations: a case study. J. Struct. Geol. 97, 93–103.
779 http://dx.doi.org/10.1016/j.jsg.2017.02.015

780 Ogiermann, J., Kalt, A., 2000. Chemical Characterization of Cordierite Breakdown Products in
781 Gneisses and Migmatites of the Schwarzwald and the Bayerische Wald. Journal of Conference
782 Abstracts 5(2), 752.

783 Ortolano, G., Visalli, R., Gaston, G., Cirrincione, R., 2018. Quantitative X-ray Map Analyser (Q-
784 XRMA): A new GIS-based statistical approach to Mineral Image Analysis. Comp. Geosci. 115, 56–
785 65. https://doi.org/10.1016/j.cageo.2018.03.001

786 Passchier, C.W., Trouw, R.A.J., 2005. Microtectonics. Springer, Berlin, Heidelberg.
787 https://doi.org/10.1007/3-540-29359-0

788 Pennacchioni, G., Guermani, A., 1993. The mylonites of the Austroalpine Dent Blanche nappe along
789 the northwestern side of the Valpelline Valley (Italian Western Alps). Memorie di Scienze Geologiche
790 45, 37–55.

791 Perego, A., Zerboni, A., Cremaschi, M., 2011. Geomorphological Map of the Messak Settafet and
792 Mellet (central Sahara, SW Libya). J. Maps 7(1), 464–475. https://doi.org/10.4113/jom.2011.1207

793 Pesenti, C., Zucali, M., Manzotti, P., Diella, V., Risplendente, A., 2012. Linking U-Th-Pb monazite
794 dating to partial melting microstructures: Application to the Valpelline series (Austroalpine domain,
795 Western Alps). Rend. Online Soc. Geol. It. 22, 183–185.

796 Ramsay, J.G., Huber, M.I., 1987. The Techniques of Modern Structural Geology: Folds and
797 Fractures. Academic Press.

798 Roda, M., Zucali, M., 2008. Meso and microstructural evolution of the Mont Morion metaintrusives
799 complex (Dent Blanche nappe, Austroalpine domain, Valpelline, Western Italian Alps). Ital. J.
800 Geosci. 127, 105–23.

801 Roda, M., Zucali, M., 2011. Tectono-metamorphic map of the Mont Morion Permian metaintrusives
802 (Mont Morion - Mont Collon - Matterhorn Complex, Dent Blanche Unit), Valpelline - Western Italian
803 Alps. J. Maps **7**, 519–535. https://doi.org/10.4113/jom.2011.1194

804 Roda, M., Zucali, M., Corti, L., Visalli, R., Ortolano, G. Spalla, M.I., 2021. Blueschist mylonitic
805 zones accommodating syn-subduction exhumation of deeply buried continental crust: The example
806 of the Rocca Canavese Thrust Sheets Unit (Sesia-Lanzo Zone, Italian Western Alps). Swiss J. Geosci.
807 114, 6–39. https://doi.org/10.1186/s00015-021-00385-7

808 Salvi, F., Spalla, M.I., Zucali, M., Gosso, G., 2010. Three-dimensional evaluation of fabric evolution
809 and metamorphic reaction progress in polycyclic and polymetamorphic terrains: a case from the
810 Central Italian Alps. In: Spalla, M.I., Marotta, A.M., Gosso, G. (Eds.), Advances in Interpretation of
811 Geological Processes, 334, 173–187. https://doi.org/10.1144/SP332.11

812 Sawyer, E.W., 2001. Melt segregation in the continental crust: distribution and movement of melt in
813 anatectic rocks. J. Metam. Geol. 19, 291–309. https://doi.org/10.1046/j.0263-4929.2000.00312.x

814 Sawyer, E.W., 2008. Working with Migmatites. Short Course Series: Mineralogical Association of
815 Canada, volume 38. Quebec: Mineralogical Association of Canada.

816 Schmid, S.M., Fügenschuh, B., Kissling, E. Schuster, R., 2004. Tectonic map and overall architecture
817 of the Alpine orogen. Eclogae Geologicae Helvetiae 97, 93–117. https://doi.org/10.1007/s00015-004-
818 1113-x

819 Seifert, F., Schreyer, W., 1970. Lower temperature stability limit of Mg cordierite in the range 1-7
820 kbar water pressure: a redetermination. Contrib. Mineral. Petrol. 27, 225–238.
821 https://doi.org/10.1007/BF00385779

822 Spalla, M.I., 1993. Microstructural control on the P-T path construction in metapelites from the
823 Austroalpine crust (Texel Gruppe, Eastern Alps). Schweizerische Mineralogische und
824 Petrographische Mitteilungen 73(2), 259–275. https://doi.org/10.5169/seals-55573

825 Spalla, M.I., Zucali, M., Di Paola, S., Gosso, G., 2005. A critical assessment of the tectono-thermal
826 memory of rocks and definition of tectono-metamorphic units: evidence from fabric and degree of
827 metamorphic transformations. Geol. Soc. Spec. Publ. 243(1), 227–247,
828 https://doi.org/10.1144/GSL.SP.2005.243.01.16

829 Spear, F., 1994. Metamorphic Phase Equilibria and Pressure-Temperature-Time Paths. Mineralogical
830 Society Monographs, 799 pp.

831 Tavani, S., Granado, P., Corradetti, A., Girundo, M., Iannace, A., Arbués, P., Muñoz, J.A., Mazzoli,
832 S., 2014. Building a virtual outcrop, extracting geological information from it, and sharing the results
833 in Google Earth via OpenPlot and Photoscan: An example from the Khaviz Anticline (Iran). Comp.
834 Geosci. 63, 44–53, http://dx.doi.org/10.1016/j.cageo.2013.10.013

835 Tavani, S., Corradetti, A., Billi, A., 2016. High precision analysis of an embryonic extensional fault-
836 related fold using 3D orthorectified virtual outcrops: The viewpoint importance in structural geology.
837 J. Struct. Geol. 86, 200–210, http://dx.doi.org/10.1016/j.jsg.2016.03.009

838 Tavani, S., Billi, A., Corradetti, A., Mercuri, M., Bosman, A., Cuffaro, M., Seers, T., Carminati, E.,
839 2022. Smartphone assisted fieldwork: Towards the digital transition of geoscience fieldwork using
840 LiDAR-equipped iPhones. Earth Sci. Rev. 227, 103969,
841 https://doi.org/10.1016/j.earscirev.2022.103969

842 Thiele, S.T., Grose, L., Samsu, A., Micklethwaite, S., Vollgger, S.A., Cruden, A.R., 2017. Rapid,
843 semi-automatic fracture and contact mapping for point clouds, images and geophysical data. Solid
844 Earth, 8, 1241–1253, https://doi.org/10.5194/se-8-1241-2017

Visalli, R., Ortolano, G., Godard, G., Cirrincione, R., 2021. Micro-Fabric Analyzer (MFA): A New Semiautomated ArcGIS-Based Edge Detector for Quantitative Microstructural Analysis of Rock Thin-Sections. ISPRS Int. J. Geo-Inf.10, 51, https://doi.org/10.3390/ijgi10020051

Waters, D.J., 2001. The significance of prograde and retrograde quartz-bearing intergrowth microstructures in partially melted granulite-facies rocks. Lithos 56, 97–110. https://doi.org/10.1016/S0024-4937(00)00061-X

Westoby, M.J., Brasington, J., Glasser, N.F., Hambrey, M.J., Reynolds, J.M., 2012. 'Structure-from-Motion'photogrammetry: A low-cost, effective tool for geoscience applications. Geomorphology 179, 300–314. https://doi.org/10.1016/j.geomorph.2012.08.021

White, R.W., Powell, R., Holland, T.J.B., Johnson, T.E., Green, E.C.R., 2014. New mineral activity–composition relations for thermodynamic calculations in metapelitic systems. J. Metam. Geol. 32, 261–286, https://doi.org/10.1111/jmg.12071

Whitney, D.L., Evans, B.W., 2010. Abbreviation for names of rock-forming minerals. Am. Mineral. 95, 185–87, https://doi.org/10.2138/am.2010.3371

Yakymchuk C., 2020. Migmatites. In: Alderton D., Elias S.A. (Eds), Enciclopedia of Geology (Second edition), Academic press, 492-501. https://doi.org/10.1016/B978-0-08-102908-4.00021-7

Zerboni, A., Perego, A., Cremaschi, M., 2015. Geomorphological map of the tadrart acacus massif and the Erg Uan kasa (Libyan central sahara). J. Maps, 11(5), 772–778, https://doi.org/10.1080/17445647.2014.955891

Zucali, M., Spalla, M.I., Gosso, G., 2002. Strain partitioning and fabric evolution As A correlation tool: the example of the eclogitic micaschists complex in the SesiaLanzo Zone (Monte Mucrone e Monte Mars, Western Alps Italy). Schweizerische Mineralogische und Petrographische Mitteilungen 82, 429–454.

Zucali, M., Manzotti, P., Diella, V., Pesenti, C., Risplendente, A., Darling, J., Engi, M. 2011. Permian tectonometamorphic evolution of the Dent-Blanche Unit (Austroalpine domain, Western Italian Alps). Rend. Online Soc. Geol. It. 15, 133–136.

Zucali, M., Corti, L., Delleani, F., Zanoni, D., Spalla, M.I., 2020. 3D reconstruction of fabric and metamorphic domains in a slice of continental crust involved in the Alpine subduction system: The example of Mt. Mucrone (Sesia–Lanzo Zone, Western Alps). Int. J. Earth Sci. 109(4), 1337–1354. https://doi.org/10.1007/s00531-019-01807-6

Zucali M., Corti, L., Roda, M., Ortolano G., Visalli, R., Zanoni, D., 2021 Quantitative X-ray Maps Analysis of Composition and Microstructure of Permian High-Temperature Relicts in Acidic Rocks from the Sesia-Lanzo Zone Eclogitic Continental Crust, Western Alps. Minerals 11, 1421. https://doi.org/10.3390/min11121421

Zucali, M., 2023. pyMinColab. Available at https://github.com/mzucali/pyMinColab/ (accessed 14 July 2023).

Figure Captions

Fig. 1: (a) Tectonic sketch map of the Alps showing the main units; (b) Geological map of the Western Alps (modified after Roda et al., 2021). E: Etirol-Lèvaz; Em: Emilius; GR: Glacier Refray; Pi: Pillonet; V: Vanoise; IIDK: II Zona Diorito-Kinzigitica.

Fig. 2. (a) Geological map of the DBTS (modified from Caso et al. 2024); (b) geological cross-section (A – A') across the Arolla and Valpelline series.

Fig. 3: (a) view of the Lac Mort area during the drone flight; (b) 3D outcrop model acquired through iPad 11" Pro equipped with LiDAR sensor; (c) point cloud of a 3D outcrop model processed in CloudCompare for the structural data extraction; (d) yellow lines traced on the Google Satellite© in Google Earth to be imported in QGIS for planes extraction.

Fig. 4: Micro-Fabric Analyzer workflow (modified after Visalli et al., 2021 and Caso, 2023).

892 **Fig. 5:** Summary of the main features of different cordierite-migmatitic gneiss samples collected in
893 different localities of the Valpelline Series.

894 **Fig. 6:** (a) S_1 foliation in a basic granulite level discordant respect to the external S_2 pervasive in
895 migmatite gneiss; (b) isoclinal F_2 affecting a brown amphibolite level; (c) isoclinal F_3 folds in
896 cordierite-migmatite gneiss; cordierite is folded and concentrated in fold hinges; (d) isoclinal F_3 folds
897 in cordierite-migmatite gneiss with local development of S_3 axial plane foliation made of sillimanite
898 and biotite, wrapping cordierite blasts; (e) asymmetric F_3 folds suggesting shearing of the short limb
899 and injection of melt along it (red arrows); (f) sheared brown amphibolite levels developing an "a-
900 type" flanking structure with leucosome as CE element; the sketch of the structure in the upper right
901 side is from Grasemann et al. (2003); (g) S_3 crenulation cleavage in migmatite gneiss; (h) two
902 pegmatitic dykes within migmatite (red arrows): the first is parallel to the S_2, the second cross-cut the
903 main and is gently folded; (i) two systems of pegmatitic dykes cross-cutting F_3 folds.

904 **Fig. 7:** (a) equal area stereographic projection (lower hemisphere; made with Stereonet 10;
905 Allmendinger et al., 2013; Cardozo and Allmendinger, 2013) of poles to S_1 foliation measured from
906 the field; (b) poles to S_1 foliations measured from LiDAR point clouds; (c) poles to S_2 foliations of
907 field data; (d) poles to S_2 foliations measured from LiDAR point cloud (blue dots with Kamb contour)
908 and from UAV point cloud (black dots); (e) A_2 fold axes (blue triangles) and axial planes (blue
909 planes); (f) projection of leucosomes discordant to the S_2 (planes measured on the field) and strikes
910 of leucosomes obtained from CloudCompare (rose diagrams); (g) poles to S_3 foliations, A_3 axes and
911 axial planes (measured on the field); (h) rose diagrams of the strikes of pegmatitic dykes measured
912 on the field; (i) pegmatite and aplites planes measured on the field; (j, k, l) dykes directions extracted
913 from LiDAR, UAV point clouds and Google Earth respectively.

914 **Fig. 8**: (a) thin section scan of the VP34 sample (XPL: crossed-polarized light); (b, c) thin section
915 scans of the 33SC sample (b is PPL: plane-polarized light; c: XPL).

916 **Fig. 9:** (a) S_2 foliation in the VP34 sample: the S_2 is marked by Sil II and Bt II (PPL); (b) quartz-
917 feldspathic domain consists of elongated Qz II and Kfs in the VP34 sample (XPL); (c) S_2 microfold
918 preserved within microlithon, whose limbs are paraller to S_3 foliation consisting of Sil III and Bt III
919 in sample 33SC (PPL); (d) Grt porphyroblasts wrapped by the S_3 foliation (XPL); (e) S_3 made of Sil
920 III and Bt III wrapping Crd blasts (XPL); (f) syn-kinematic (to S_3) flattened Grt porphyroblast
921 wrapped by the S_3 foliation, showing an internal foliation in the rim concordant with the external S_3,
922 made of sillimanite (XPL).

923 **Fig. 10**: Blastesis vs. deformation diagram of cordierite-migmatite gneiss.

924 **Fig. 11:** (a, b) mineral grain maps of the samples 33SC and VP34 respectively, obtained from the
925 MFA toolbox; maps highlighting quarz-feldspathic domains in yellow are reported at the right and at
926 the bottom respectively; (c) modal percentages of both samples obtained from the first cycle of Q-
927 XRMA.

928 **Fig. 12:** (a) Long axis orientation rose diagrams for the main phases occurring in the two analysed
929 samples; (b, c, d, e) long axis orientations maps of sillimanite, biotite, quartz and K-feldspar in sample
930 VP34; f) long axis orientation map of sillimanite in sample 33SC (modified from Caso, 2023); (g)
931 detail of figure f, showing a microdomains where the overprinting relationship between S_2 and S_3 are
932 visible from long axis sillimanite orientation; in the bottom left the rose diagram shows data only of
933 this zoom.

934 **Fig. 13:** (a) Roundness map of quartz and K-feldspar in sample VP34; (c) width/length ratio
935 (roundness) of quartz grains in the sample VP34; (d) long axis orientation map of garnet grains in the
936 sample 33SC; (e) roundness map of garnet in sample 33SC; (f) width/length ratio (roundness) of
937 garnet grains in the sample 33SC.

938 **Fig. 14:** (a) Mg apfu calibrated map of biotite; (b) Fe apfu calibrated map of biotite; (c) #Mg vs Ti
939 apfu data of biotite extracted from each pixel of the calibrated map (black dots) and EMPA analyses

940 (discriminated on their microstructural positions) used for calibration with Q-XRMA (pink symbols);
941 (d) Ti apfu calibrated map of biotite; (e) Mg apfu calibrated map of garnet; (f) Fe apfu calibrated map
942 of garnet.

943 **Fig. 15:** Synoptic table summarizing the main features of the tectono-metamorphic stages defined in
944 the Valpelline Series.

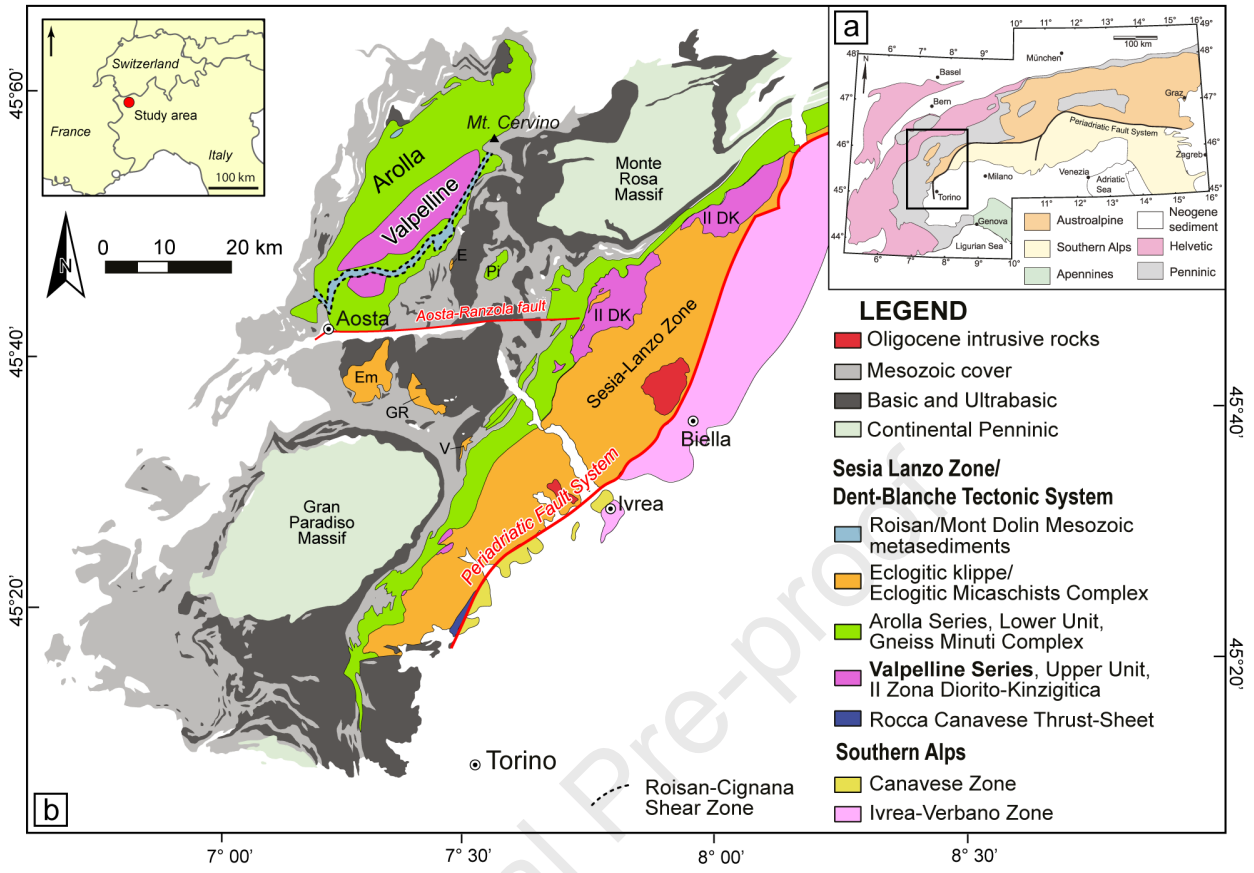

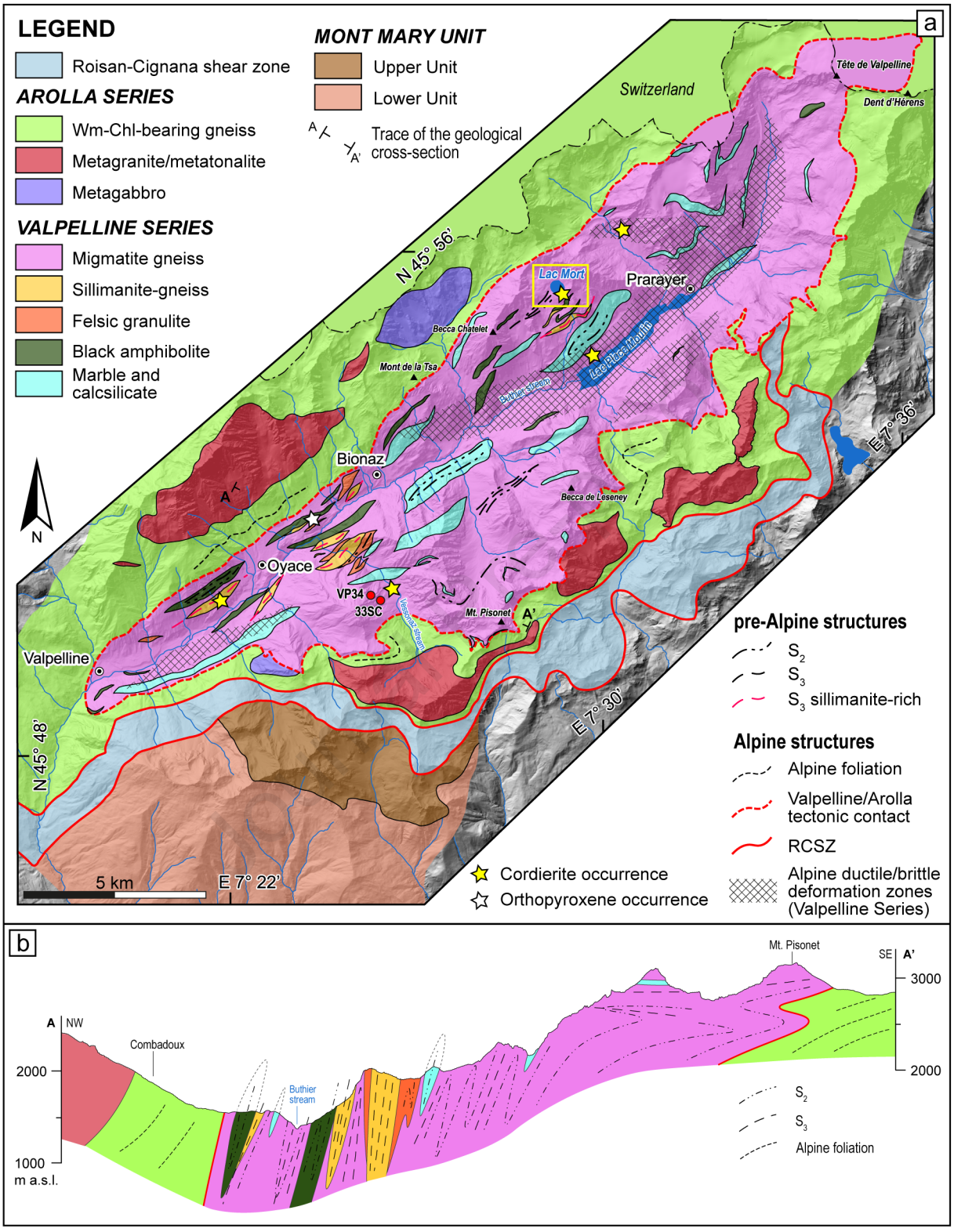
LEGEND
Roisan-Cignana shear zone
AROLLA SERIES
Wm-Chl-bearing gneiss
Metagranite/metatonalite
Metagabbro
VALPELLINE SERIES
Migmatite gneiss
Sillimanite-gneiss
Felsic granulite
Black amphibolite
Marble and calcsilicate
MONT MARY UNIT
Upper Unit
Lower Unit
Trace of the geological cross-section
a
Switzerland
Tête de Valpelline
Dent d'Hérens
N 45° 56'
Lac Mort
Prarayer
Becca Chatelet
Mont de la Tsa
Lac Place Moulin
Buthier stream
E 7° 36'
Bionaz
Becca de Leseney
A
N
Oyace
VP34
33SC
Mt. Pisonet
A'
Valpelline
N 45° 48'
E 7° 30'
5 km
E 7° 22'
pre-Alpine structures
S2
S3
S3 sillimanite-rich
Alpine structures
Alpine foliation
Valpelline/Arolla tectonic contact
RCSZ
Alpine ductile/brittle deformation zones (Valpelline Series)
Cordierite occurrence
Orthopyroxene occurrence
b
A
NW
Combadoux
2000
1000
m a.s.l.
Buthier stream
Mt. Pisonet
SE
A'
3000
2000
S2
S3
Alpine foliation

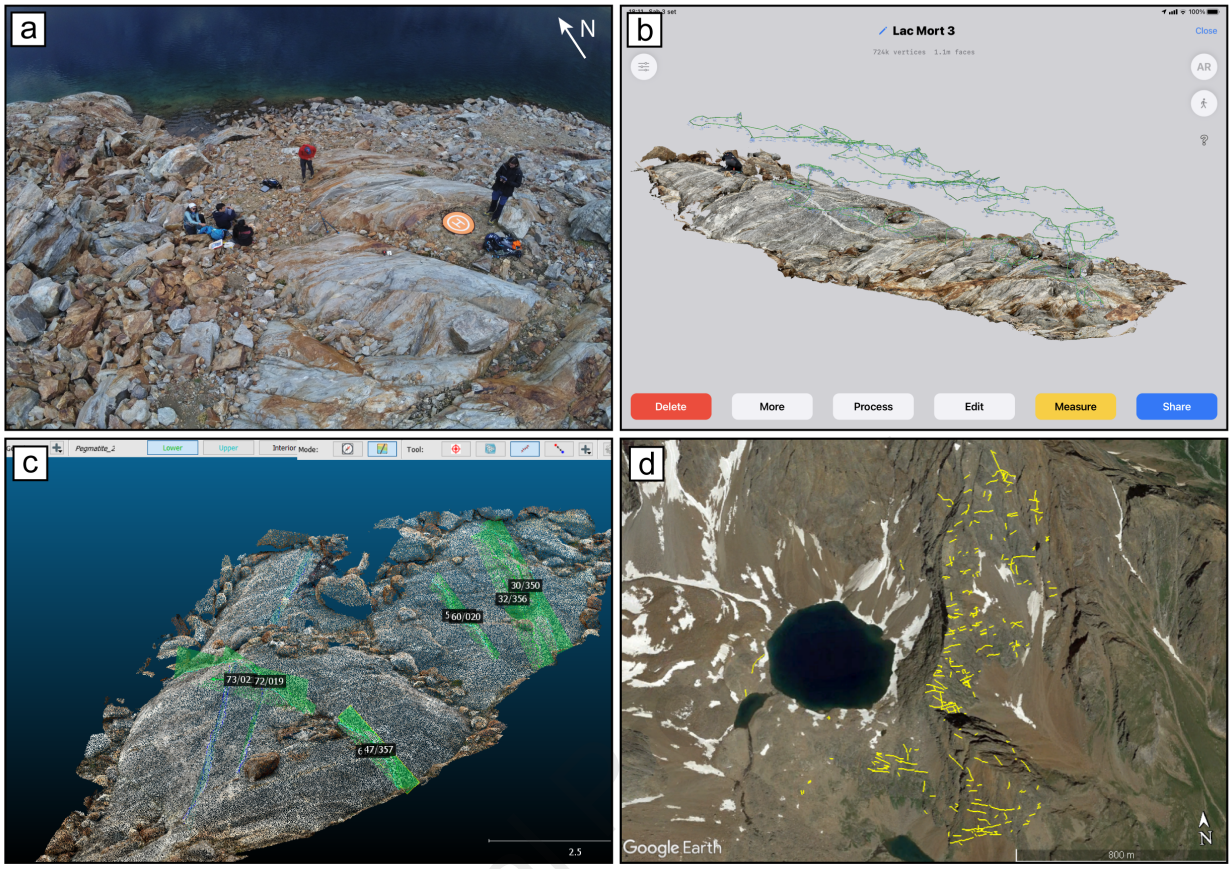
a
N
b
Lac Mort 3
724k vertices 1.1m faces
Close
AR
Delete
More
Process
Edit
Measure
Share
c
Pegmatite_2
Lower
Upper
Interior
Mode:
Tool:
30/350
32/356
60/020
73/02
72/019
47/357
2.5
d
Google Earth
800 m
N

The Micro-Fabric Analyzer

INPUTS

High-resolution optical scan

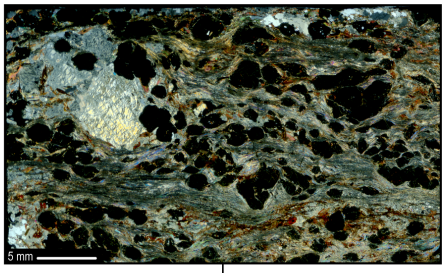

X-ray maps

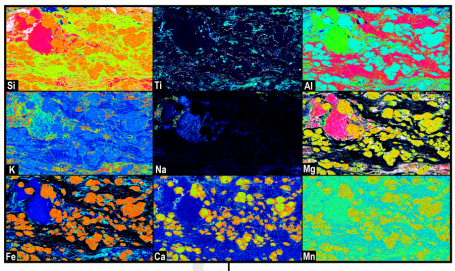

GSD
Vectorisation of rock-forming grains
(i.e., grain-boundary map)

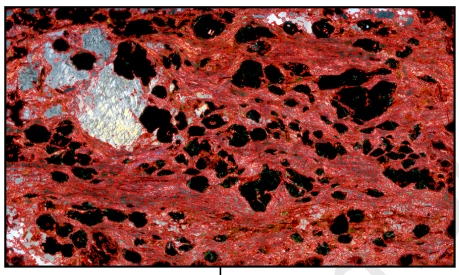

Q-XRMA
Mineral classification
(i.e., rock-forming mineral map)

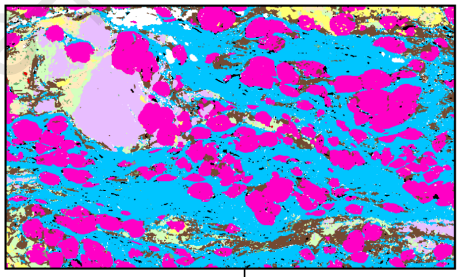

Images georeferencing
(in ArcGIS)

Min-GSD
Mineralogical subdivision of digitised grains

OUTPUTS

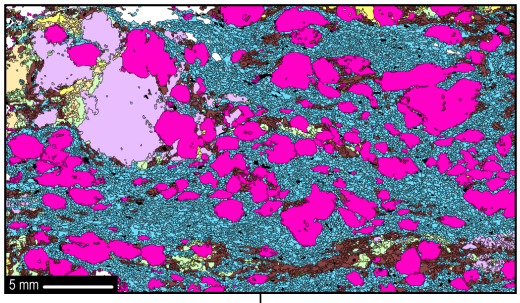

- Mineral grain boundaries
- Mineral grain-size descriptors
- Mineral grain shape factors
- Mineral abundances

Sample	*Crd-locality*	*WGS coordinates*	*main features*	
22CBP10	Grand Place, d'Orein stream	7.5035526 45.9372687	Foliation defined by Bt. Crd is strongly pinitised.	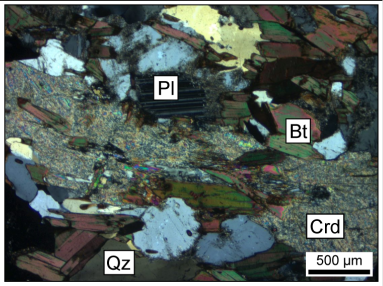
6CP 29SC 31SC 38SC	N of Lac Mort S of Lac Mort S of Lac Mort S of Lac Mort	7.4827177 45.9213619 7.4860345 45.9189366 7.48707993 45.91875192 7.48600577 45.91895677	Foliation defined by Bt and locally minor fibrous Sil. Crd is strongly pinitised	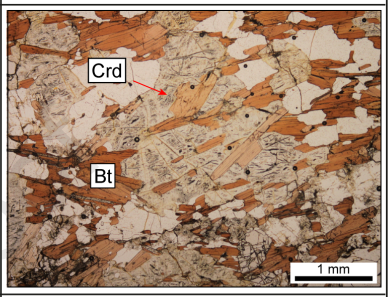
I_22_07 I_28_07	Lac Place Moulin Lac Place Moulin	7.4991744 45.9032835 7.506861 45.907447	Foliation defined by Bt and minor Sil. Crd is strongly pinitised	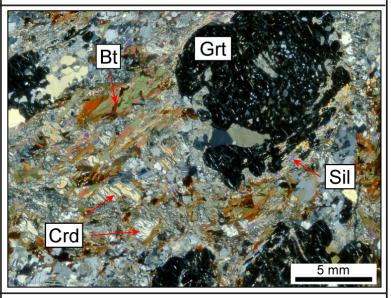
22FC17A	Localitè La Ruine	7.364324 45.839654	Foliation defined by Bt and minor Sil. Crd is strongly pinitised	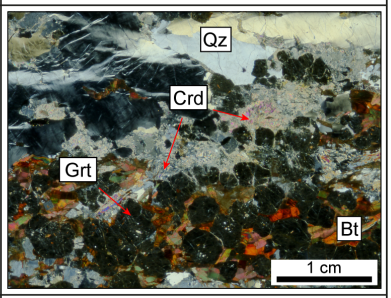
VP34 VP44 33SC	Comba Vessonaz Comba Vessonaz Comba Vessonaz	7.4238788 45.8425377 7.4236035 45.8424476 7.4268945 45.8418167	Foliation defined by Sil and Bt. Crd idiomoprhic and always well preser-ved.	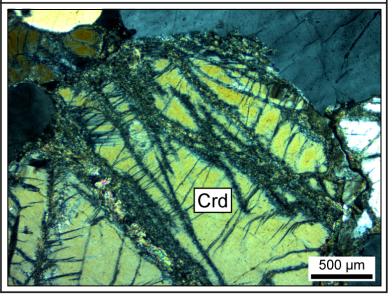

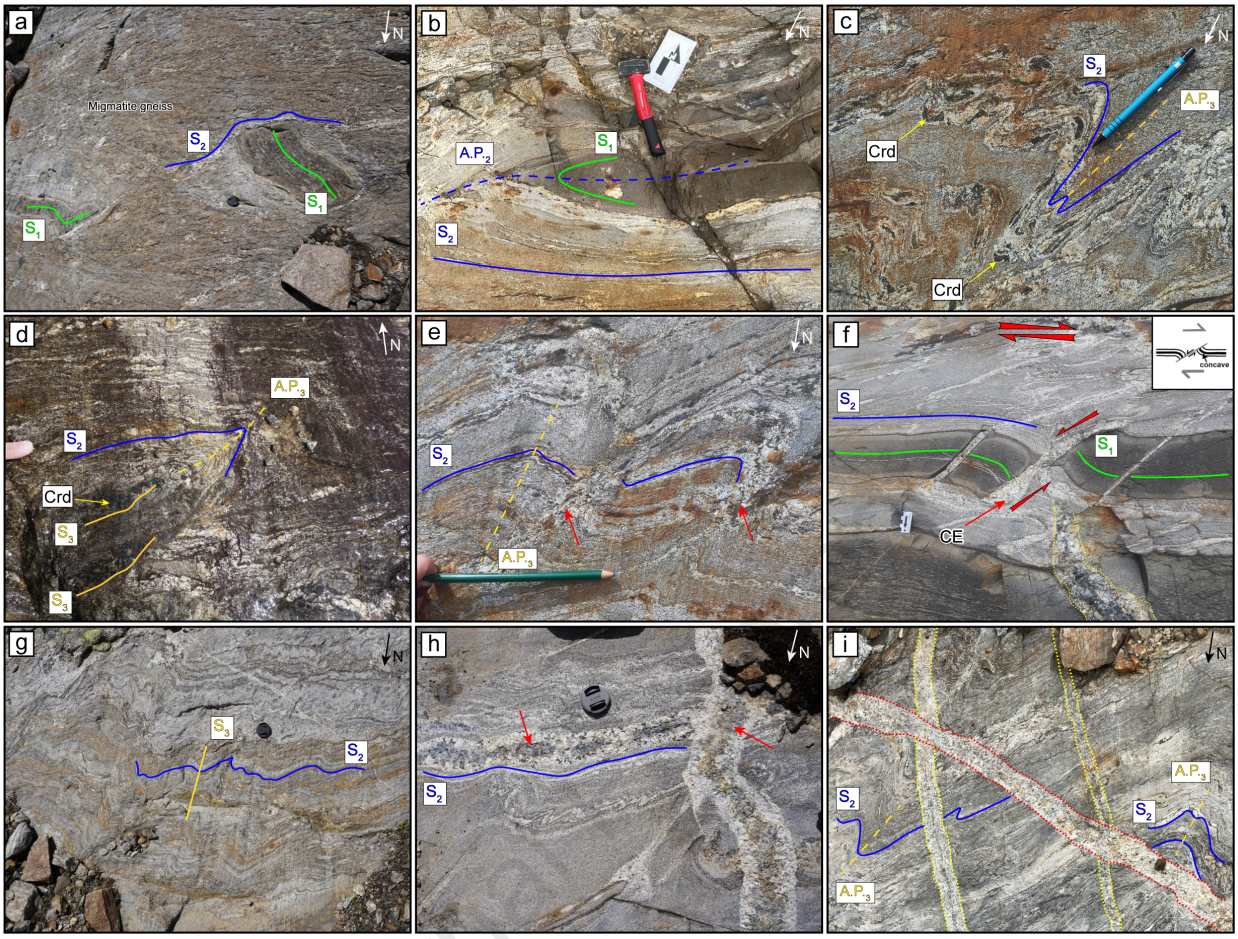

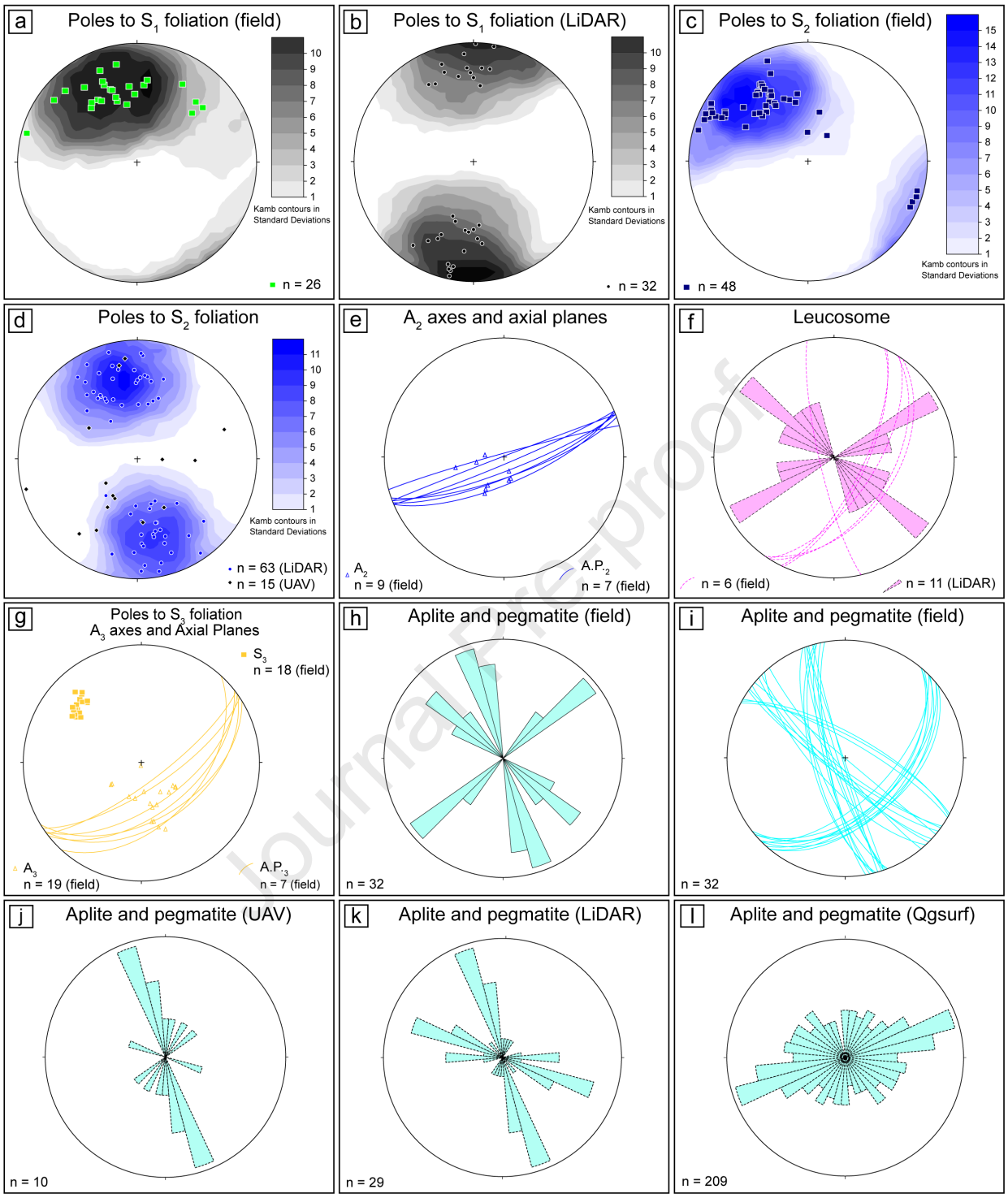

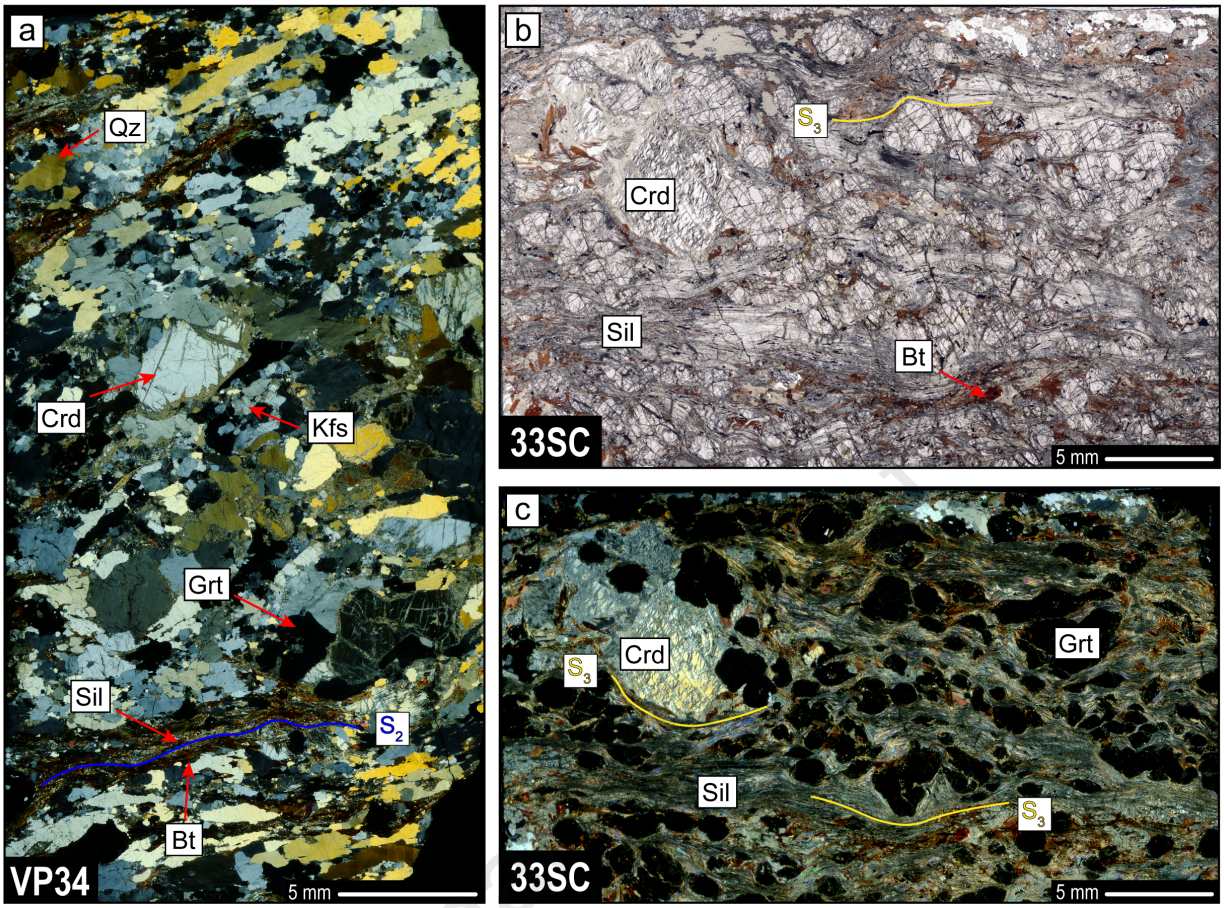

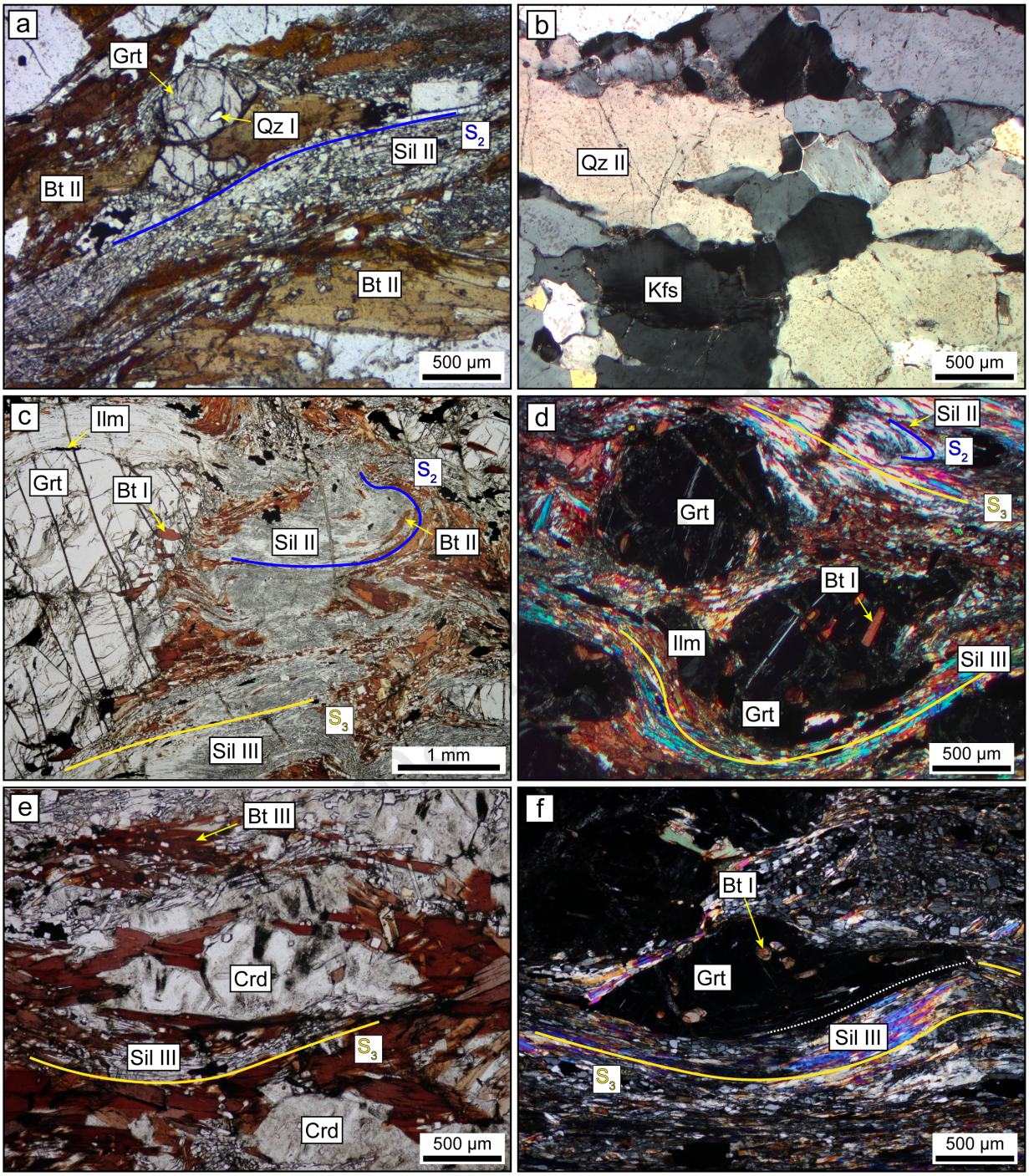
a
Grt
Qz I
Sil II
S_2
Bt II
Bt II
500 µm
b
Qz II
Kfs
500 µm
c
Ilm
Grt
Bt I
S_2
Sil II
Bt II
S_3
Sil III
1 mm
d
Sil II
S_2
S_3
Grt
Bt I
Ilm
Sil III
Grt
500 µm
e
Bt III
Crd
Sil III
S_3
Crd
500 µm
f
Bt I
Grt
Sil III
S_3
500 µm

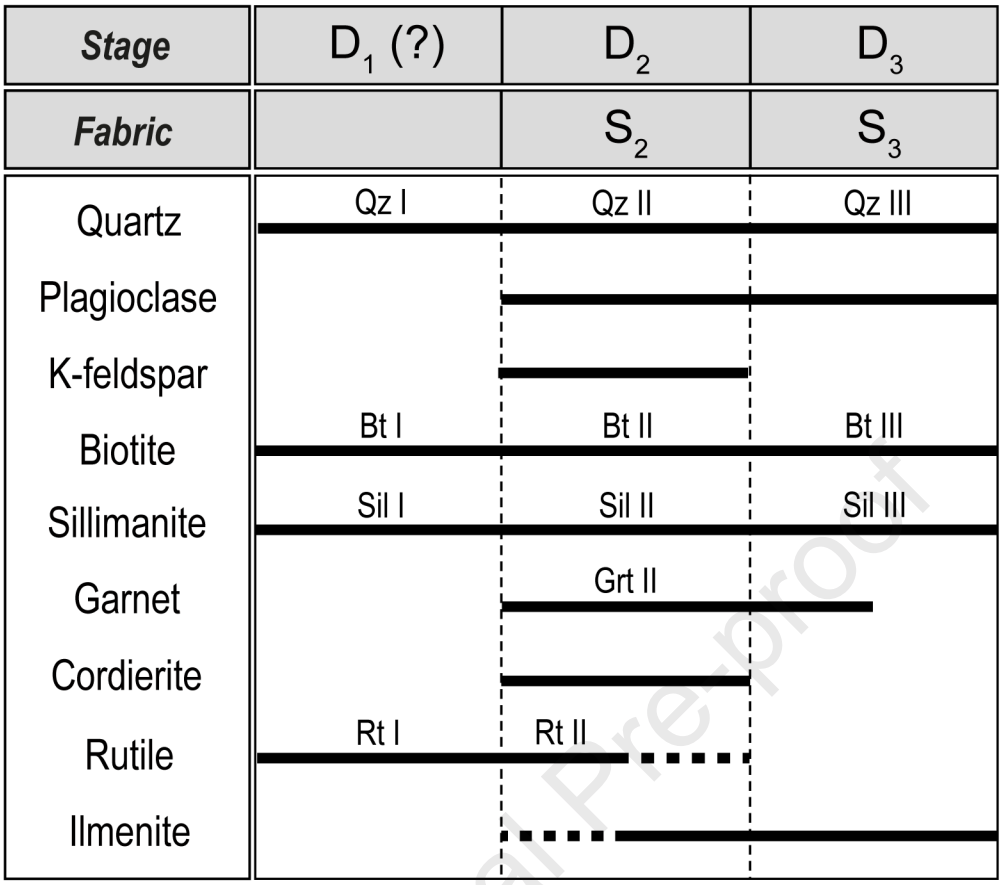

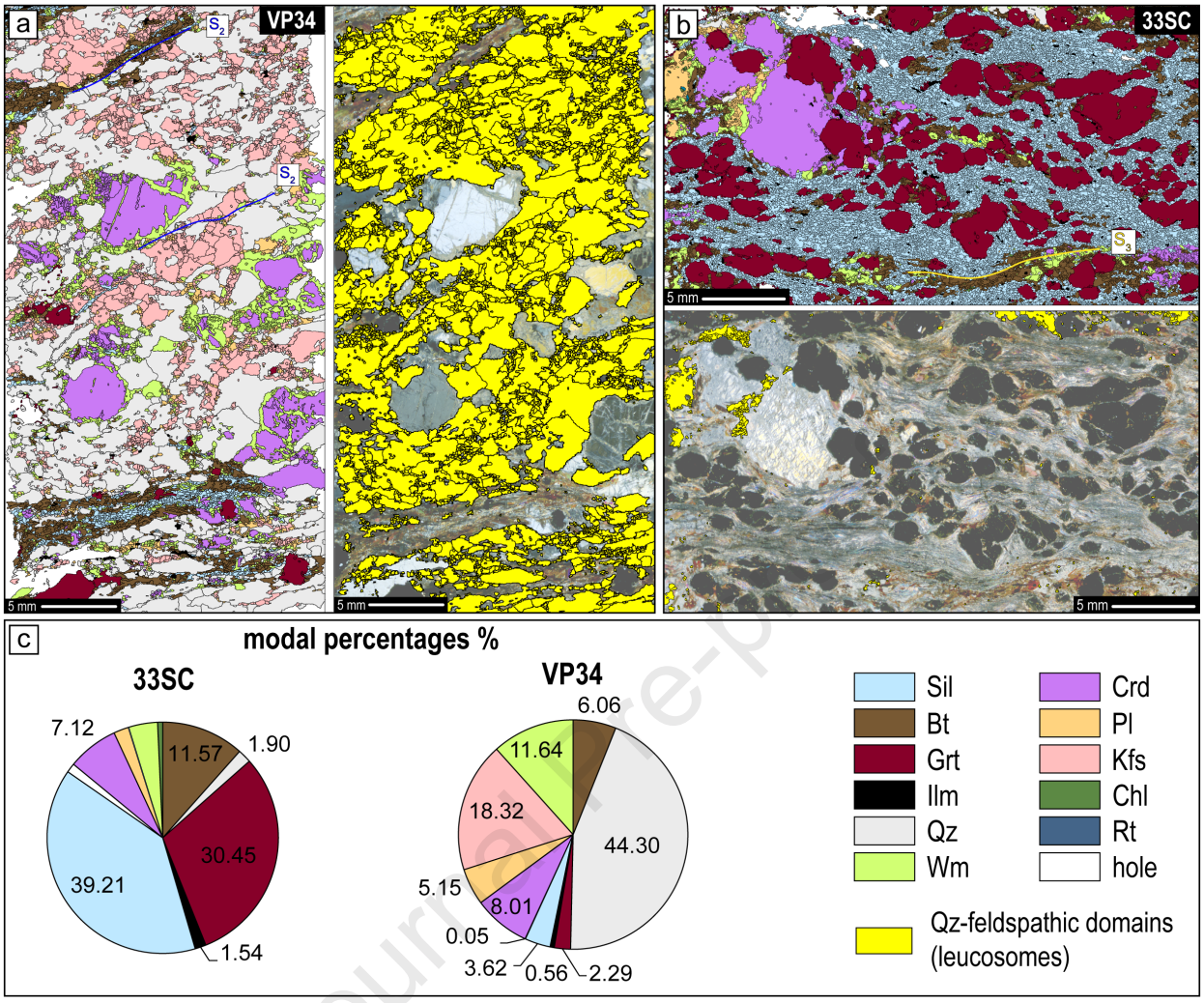

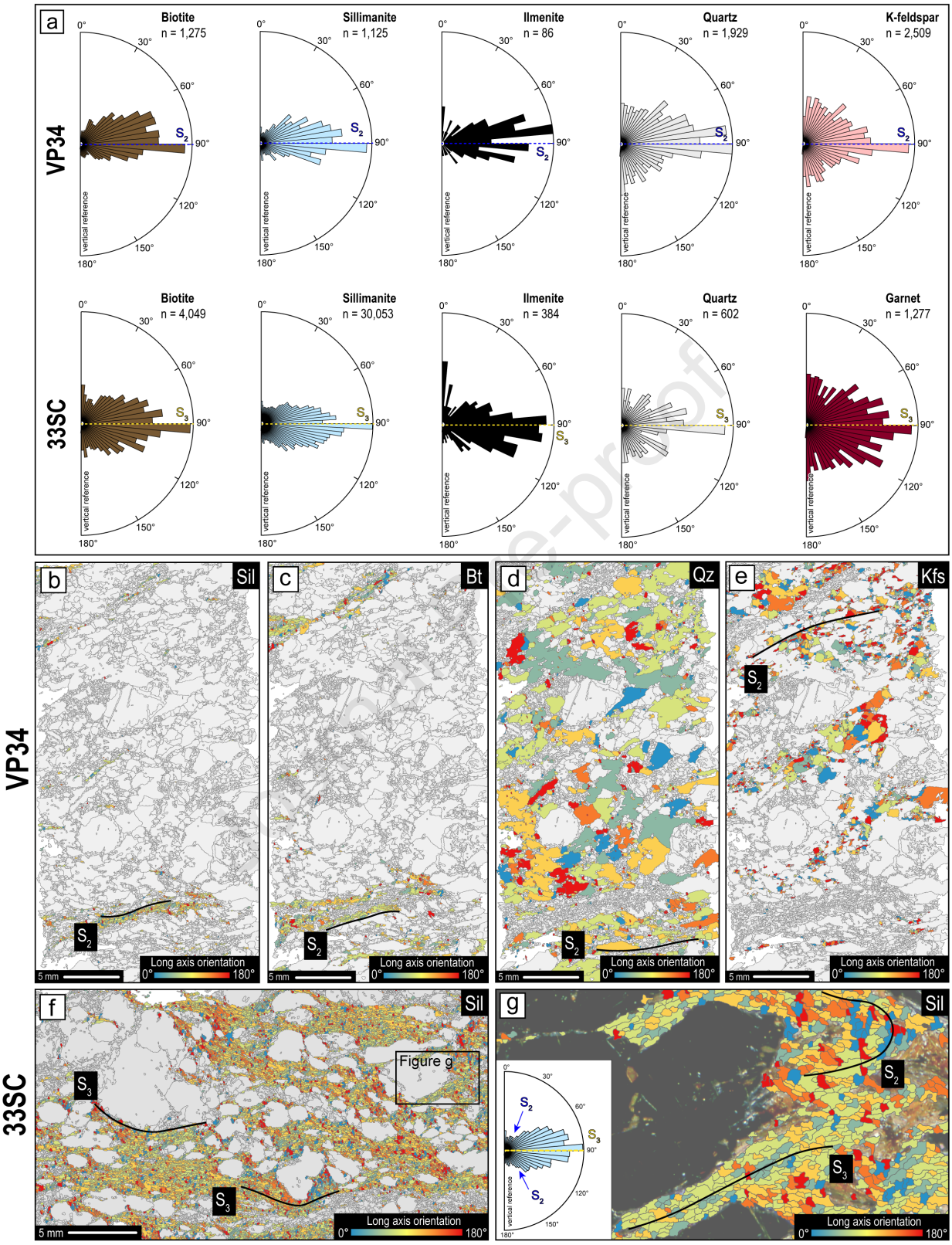
a
VP34
Biotite
n = 1,275
Sillimanite
n = 1,125
Ilmenite
n = 86
Quartz
n = 1,929
K-feldspar
n = 2,509
33SC
Biotite
n = 4,049
Sillimanite
n = 30,053
Ilmenite
n = 384
Quartz
n = 602
Garnet
n = 1,277
vertical reference
b
Sil
c
Bt
d
Qz
e
Kfs
Long axis orientation
0°
180°
5 mm
f
Figure g
g

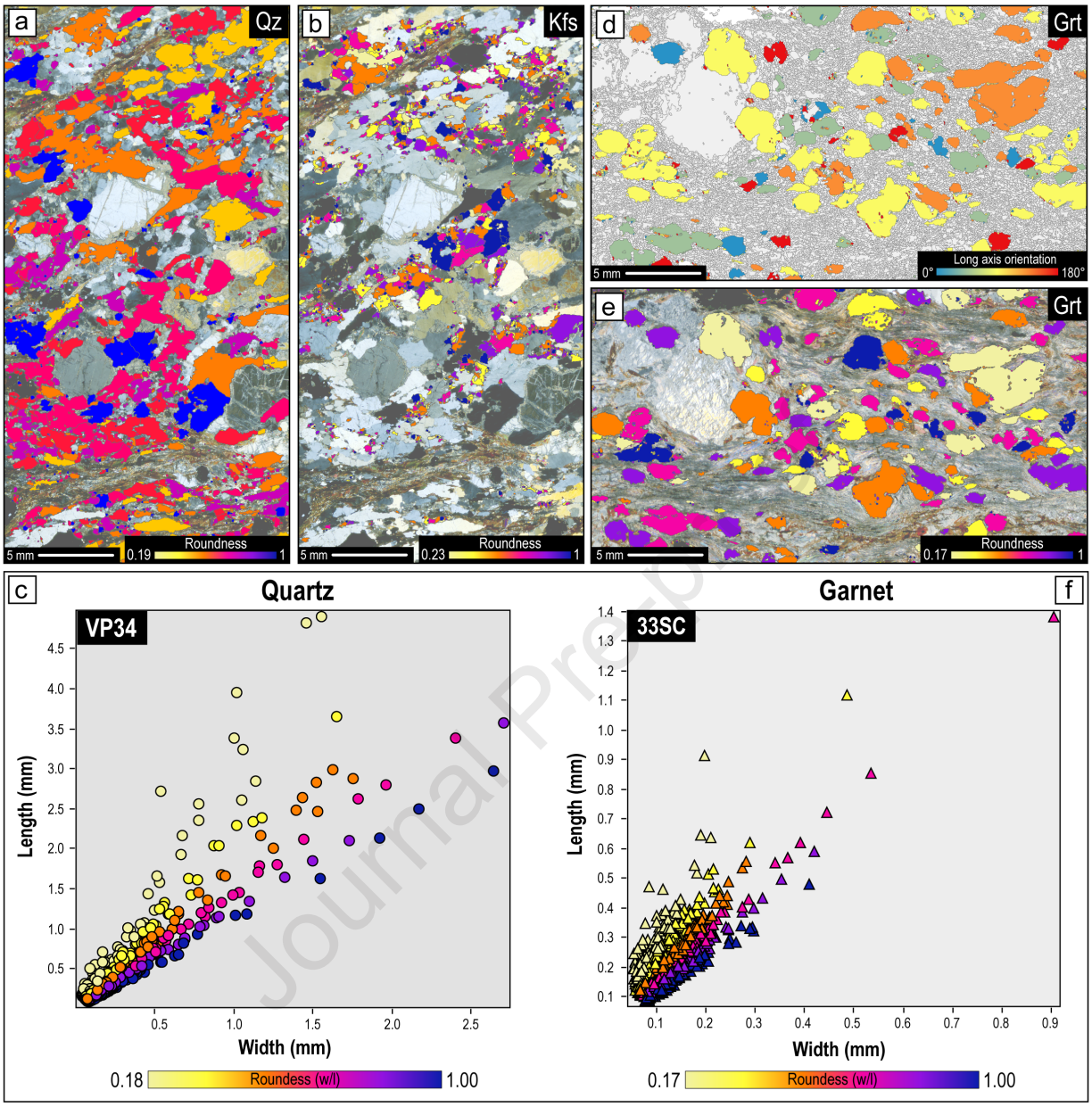

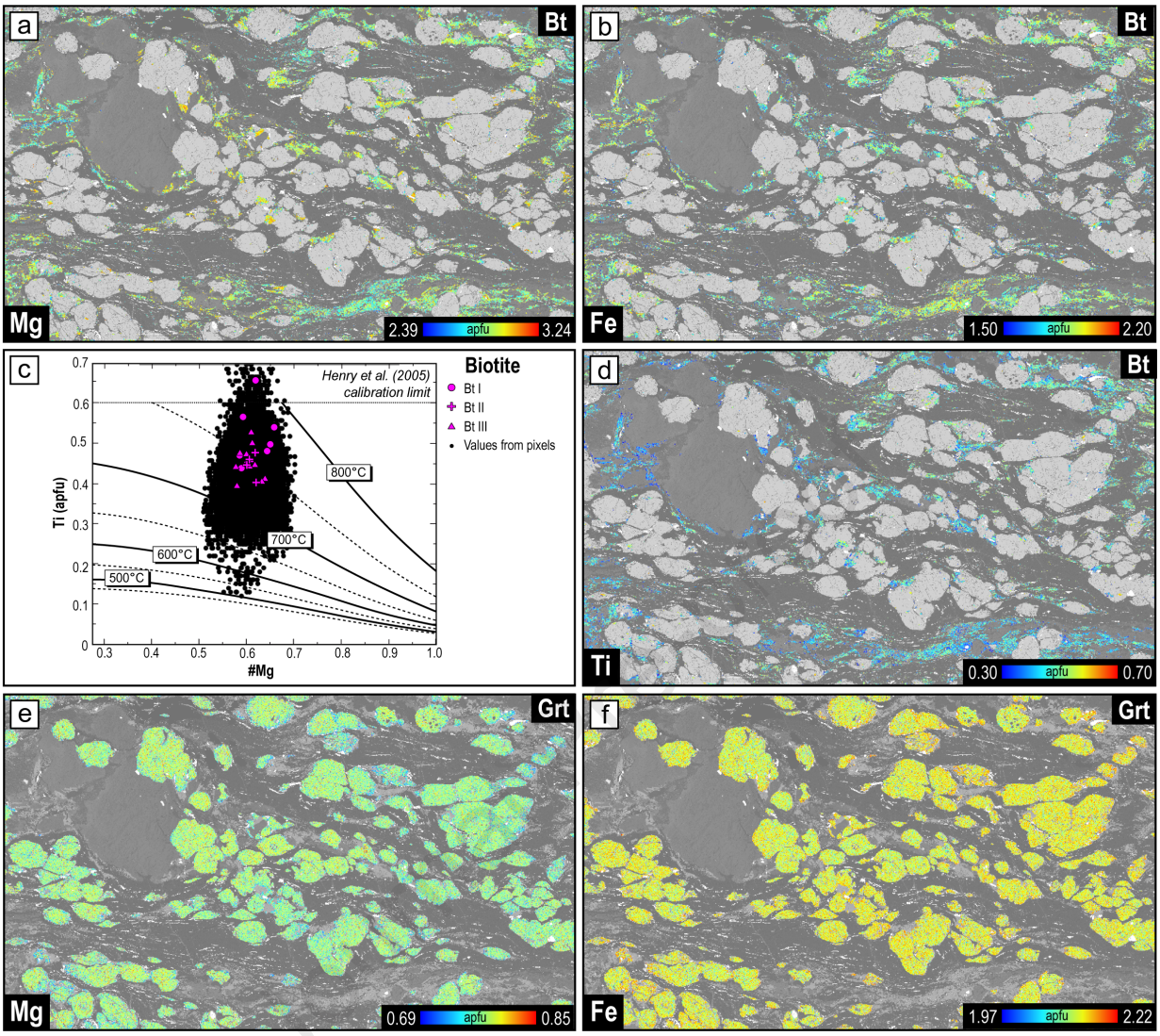
a
Bt
Mg
2.39
apfu
3.24
b
Bt
Fe
1.50
apfu
2.20
c
Henry et al. (2005)
calibration limit
Biotite
Bt I
Bt II
Bt III
Values from pixels
800°C
700°C
600°C
500°C
Ti (apfu)
#Mg
d
Bt
Ti
0.30
apfu
0.70
e
Grt
Mg
0.69
apfu
0.85
f
Grt
Fe
1.97
apfu
2.22

D_1	D_2	early D_3	late D_3
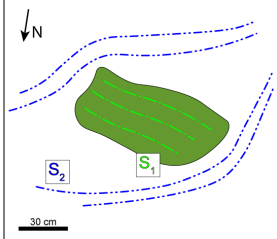	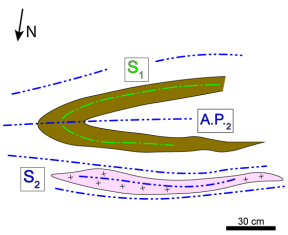	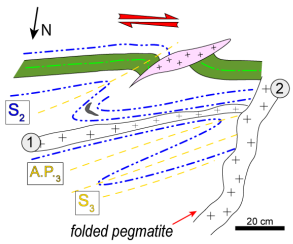	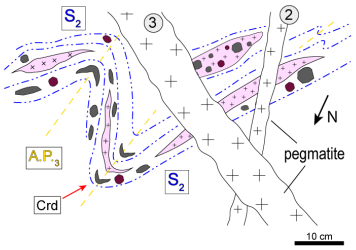
S_1 foliation in basic granulite and brown amphibolite Discordant to the S_2 foliation of migmatites	Isoclinal folding of the S_1 foliation and trasposition Development of S_2 axial plane foliation Melt production = leucosomes marking S_2.	Isoclinal to asymmetric close folds with top-to-the W shearing Local development of S_3 axial plane foliation Cordierite makes deformed aggregates in fold hinges Pegmatitic dykes start intrude migmatites and are locally folded.	Different systems of pegmatitic dykes cross-cutting each other and all the migmatitic structures Three systems: 1) parallel to the S_2 foliation, affected by boudinage 2) striking NNW-SSE, locally folded; 3) striking NW-SE, cross-cutting all the previous ones
Metabasite: Opx + Cpx + Pl Migmatite: Bt I + Sil I + Qz I	Bt II + Sil II + **Grt** + **Crd** + **melt**	Bt III + Sil III + Ilm ± Grt	

Basic granulite | Brown amphibolite | Leucosomes | Pegmatitic dykes | Grt | folded Crd | Crd

Highlights:

- Combination of traditional field-based and remote-sensing derived structural analysis
- Extraction of structural data from LiDAR and UAV-derived 3D outcrop models
- Quantitative microstructural analysis and shape parameters extraction from vectorised grains
- Combination of quantitative meso- and microstructural analysis with mineral-chemical data
- Multiscale structural analysis applied to the Valpelline Series (Dent-Blanche Nappe)

Declaration of competing interest

The authors declare that they have no competing financial interests or personal relationships that could have appeared to influence the work reported in this paper.